

Abstract

The usage of cobalt (Co) as binder phase material in cemented carbides has been questioned because of the potential health hazards associated with cobalt particle inhalation. Cobalt is used because of its excellent adhesive and wetting properties, combined with adequate mechanical properties. The purpose of this work is to investigate the mechanical properties of Fe-Ni bulk alloys and WC-Co cemented carbides using Integrated Computational Materials Engineering (ICME) methods combined with FEM data. The report investigates the mechanical properties of several bulk alloys in the Fe-Ni system as a function of void size and fraction. FEM indentation and FEM fracture data is interpolated and used to model the hardness H and fracture toughness K_{Ic} . A precipitation hardening model based on the Ashby-Orowan's equation is implemented to predict the effect on the yield strength from precipitated particles. A model for solid solution hardening is also implemented. Existing models are used to simulate the properties of WC-Co cemented carbides together with the solid solution hardening model. Results show that the simulated properties of the Fe-Ni bulk alloys are comparable to those of cobalt. However, the results could not be confirmed due to a lack of experimental data. The properties of WC-Co cemented carbides are in reasonable agreement with existing experimental data, with an average deviation of the hardness by 11.5% and of the fracture toughness by 24.8%. The conclusions are that experimental data for different Fe-Ni bulk alloys is needed to verify the presented models and that it is possible to accurately model the properties of cemented carbides.

Sammanfattning

Användandet av kobolt (Co) som bindefas-material i hårdmetall har blivit ifrågasatt som en följd av de potentiella hälsoriskerna associerade med inhalering av koboltpartiklar. Kobolt används på grund av dess utmärkta vidhäftande och vätande egenskaper, kombinerat med tillräckliga mekaniska egenskaper. Syftet med detta arbete är att undersöka de mekaniska egenskaperna hos Fe-Ni bulklegeringar och WC-Co hårdmetall genom att använda Integrated Computational Materials Engineering (ICME) metoder kombinerat med FEM-data. Rapporten undersöker de mekaniska egenskaperna hos flera bulklegeringar i Fe-Ni systemet. FEM-indentering och FEM-fraktur data interpoleras och används för att modellera hårdheten H och brottsegheten K_{Ic} . En modell för utskilningshårdning baserad på Ashby-Orowans ekvation implementeras för att förutsäga effekten på brottgränsen av utskiljda partiklar. Även en modell för lösningshårdning implementeras. Existerande modeller används för att simulera egenskaperna hos WC-Co hårdmetall tillsammans med modellen för lösningshårdning. Resultaten visar att de simulerade egenskaperna hos Fe-Ni bulklegeringar är jämförbara med de för kobolt. Dock kan de inte bekräftas på grund av avsaknad av experimentell data. Egenskaperna hos WC-Co hårdmetall stämmer rimligt överens med existerande experimentell data, med en genomsnittlig avvikelse av hårdheten med 11.5% och av brottsegheten med 24.8%. Slutsatserna är att det behövs experimentell data för Fe-Ni bulklegeringar för att kunna verifiera modellernas noggrannhet och att det är möjligt att förutsäga egenskaperna hos hårdmetall.

Table of contents

| | | |
|----------|--|-----------|
| 1 | Introduction | 1 |
| 2 | Background | 2 |
| 2.1 | Integrated Computational Materials Engineering | 2 |
| 2.2 | Cemented carbides | 2 |
| 2.2.1 | Cobalt in cemented carbides | 3 |
| 2.2.2 | Alternative binders | 4 |
| 2.3 | Fracture toughness | 5 |
| 2.3.1 | Fracture in bulk alloys | 5 |
| 2.3.2 | Fracture in cemented carbides | 6 |
| 2.4 | Hardness | 7 |
| 2.4.1 | Solid solution hardening (SSH) | 7 |
| 2.4.2 | Precipitation hardening | 8 |
| 3 | Method | 9 |
| 3.1 | General limitations | 9 |
| 3.2 | Computational tools | 9 |
| 3.2.1 | Softwares and databases | 9 |
| 3.2.2 | Finite Element Method (FEM) | 9 |
| 3.3 | Hardness model | 10 |
| 3.3.1 | Bulk alloy hardness | 10 |
| 3.3.2 | Cemented carbide hardness | 11 |
| 3.3.3 | Solid solution hardening model | 11 |
| 3.3.4 | Bulk alloy precipitation hardening model | 12 |
| 3.4 | Fracture toughness model | 13 |
| 3.4.1 | Bulk alloy fracture toughness | 13 |
| 3.4.2 | Cemented carbide fracture toughness | 14 |
| 3.5 | Optimizing material properties | 15 |
| 4 | Results | 16 |
| 4.1 | Fracture toughness model verification | 16 |
| 4.2 | Bulk alloys | 17 |
| 4.2.1 | Material #1: Pure cobalt | 18 |
| 4.2.2 | Material #2: 45Ni/Fe | 19 |
| 4.2.3 | Material #3: Invar alloy | 20 |
| 4.2.4 | Material #4: 45Ni/Fe with C and Ti | 21 |
| 4.3 | Cemented carbides | 23 |
| 4.3.1 | WC-Co cemented carbides | 23 |
| 5 | Discussion | 27 |
| 5.1 | Bulk alloys | 27 |
| 5.2 | Cemented carbides | 27 |
| 5.3 | Environmental aspects | 28 |
| 6 | Conclusions | 30 |
| 6.1 | Recommendations | 30 |
| 7 | Acknowledgments | 30 |
| 8 | References | 31 |
| 9 | Appendix: Coefficients from FEM simulations | 33 |

1 Introduction

Cemented carbides are a type of material consisting of a hard carbide phase and a ductile binder phase. Since the invention of cemented carbides, cobalt has been used as the primary material for the binder phase. Recent studies have shown that there might be a connection between cobalt powder inhalation and an increased risk of pulmonary cancer amongst other diseases [1]. This is creating risks for workers in the cobalt mining industry. Furthermore, workers are often subjected to poor working conditions with little attention being paid to personal safety and health [2].

Other materials have been investigated and proposed as candidates for replacing cobalt [3,4] with promising results in the Fe-Ni-Co system. Finding bulk alloys that have similar or better properties than those of cobalt might influence the choice of binder material for cemented carbides in the future.

A large part of this report is based on using pre-existing models that have been verified experimentally. Thus its importance lies not in verifying that they are accurate, but rather in investigating if they can be combined to create optimization tools. The focus will be on the fracture toughness, since models that accurately predict the hardness already exist [5].

The main goal of this work is not to find materials that can substitute cobalt as primary binder phase in cemented carbides. That approach would be futile since there are many more aspects to the problem than what is in the scope of this work. Rather, the overall goal is to investigate if it is possible to use a Materials Design approach to model specific properties of certain materials. To reach that goal, it is subdivided into milestones that include

- developing and implementing models that can predict the properties of bulk alloys as a function of void size and spacing
- investigating the properties of Fe-Ni bulk alloys in comparison with pure cobalt
- optimizing the product of hardness and toughness
- predicting the properties of cemented carbides as a function of carbide grain size and binder fraction.

The work aims at answering the questions

- Can the properties of investigated materials be predicted with the used models?
- What is the relative effect of precipitation hardening and solid solution hardening?
- How accurately can WC-Co cemented carbide properties be predicted by combining the presented models?

2 Background

2.1 Integrated Computational Materials Engineering

Integrated Computational Materials Engineering (ICME) is a relatively new method for materials engineering. The term is broad and involves all types of materials engineering that mainly use computational methods as opposed to experimental ones [6]. ICME has a strong potential for allowing engineers to perform simulation-based optimization and development of materials. The traditional method of trial and error is usually costly, both in terms of time and money. Thus the main goal of ICME is to shorten the time from the drawing table to having a new material.

In the Ph.D. thesis by Martin Walbrühl [7], an attempt was made to model the hardness of multicomponent binders using an ICME approach. In the thesis, focus was placed on the solid solution hardening of multicomponent systems. The results showed that the method can be used to accurately predict the hardness of classical binders as well as possible alternative systems.

2.2 Cemented carbides

The material class cemented carbides contains materials that consist of a binder phase with a relatively high toughness combined with at least one hard carbide phase [7]. The term "cemented" refers to the fact that the binder phase acts as a cement around the carbides. The materials are produced by powder metallurgy and liquid phase sintering. Tungsten carbide (WC) is normally used as the carbide phase. Other popular carbides are titanium carbide (TiC) and tantalum carbide (TaC) [8]. The most widely used binder in cemented carbides is cobalt. The major areas of usage are in tools for steel turning and machining, normally coated with other carbides or ceramic materials, in drilling tools in the gas, oil and mining industries, and for parts that require high wear resistance [4].

Two of the most important mechanical properties of cemented carbides are the fracture toughness K_{Ic} (MPa m^{1/2}) and the hardness H (MPa). The two properties follow an inverse relation for most materials, i.e. as one increases the other one tends to decrease. A main concern for the cemented carbide industry is to maximize hardness while maintaining a fracture toughness at acceptable levels [9]. Generally, fracture toughness is a more complex property to evaluate and measure.

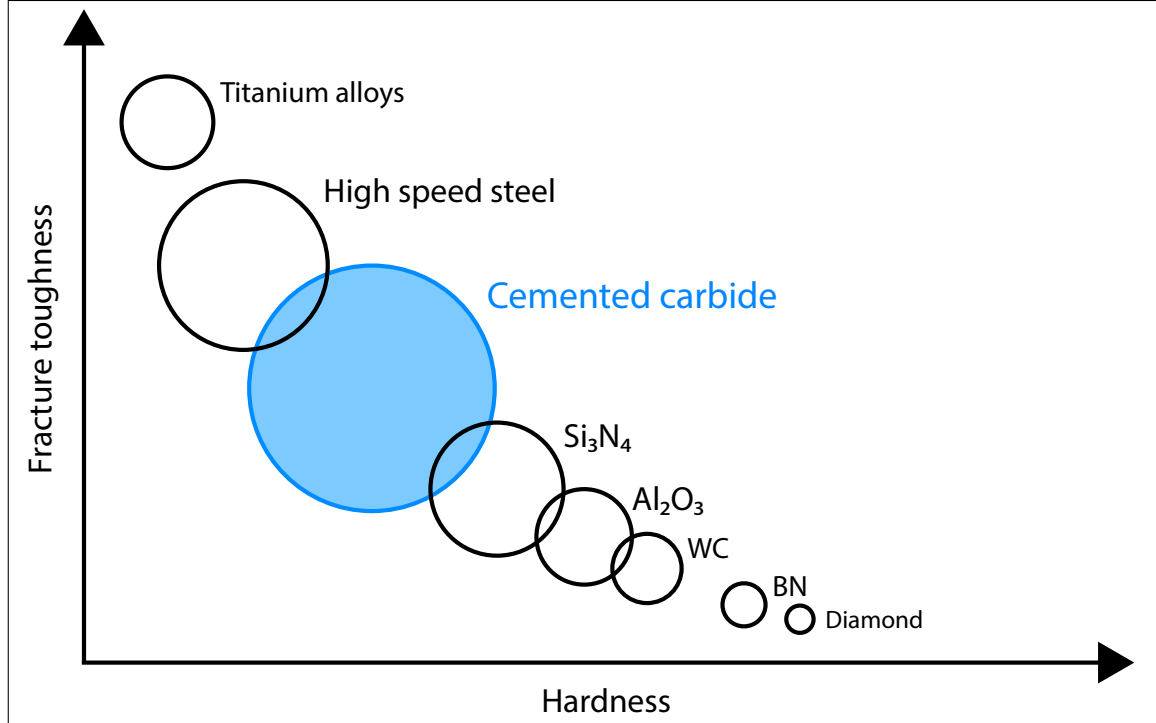


Figure 1: The figure shows the inverse relation between hardness and fracture toughness for common materials. Cemented carbides display a unique combination of both properties.

2.2.1 Cobalt in cemented carbides

The cemented carbide industry has since its initial development during the early 1920's been heavily influenced by the usage of cobalt as the primary binder material [8]. There are many prerequisites for the binder phase material. It needs to be tough and ductile enough to withstand heavy stress without cracking, at the same time as having a relatively high hardness. It also needs to have good wetting and adhesion to carbide grains. Cobalt has shown to provide all of these qualities, making it a suitable material [4].

The cobalt binder in cemented carbides is more accurately a Co-W-C alloy because of the solution of tungsten and carbon atoms into the liquid binder during sintering. Sintering normally takes place in the temperature range 1623-1923 K [10]. Upon solidification, the phase transformation from liquid to FCC takes place and the tungsten and carbon atoms form a solid solution together with cobalt. One very important thermodynamical aspect in the production of WC-Co cemented carbides is the amount of carbon [3]. If the content is too low, the M_6C or $M_{12}C$ phase may become stable and if the carbon content is too high, graphite may be present. Neither of the mentioned phases are normally desired [10]. The carbon content at which only WC and FCC will be present depends on the volume fraction of the binder. For a WC-10vol%Co cemented carbide, FCC and WC will be present for a mass percentage of 5.61-5.71 of carbon as described in figure 2. The equilibrium transformation from FCC to the low temperature phase HCP of the cobalt binder takes place at approximately 700 K. However, the dissolution of tungsten and especially carbon into the binder matrix stabilizes the FCC phase by lowering the transformation temperature [4]. Thus the FCC structure of the cobalt binder normally remains after cooling to room temperature.

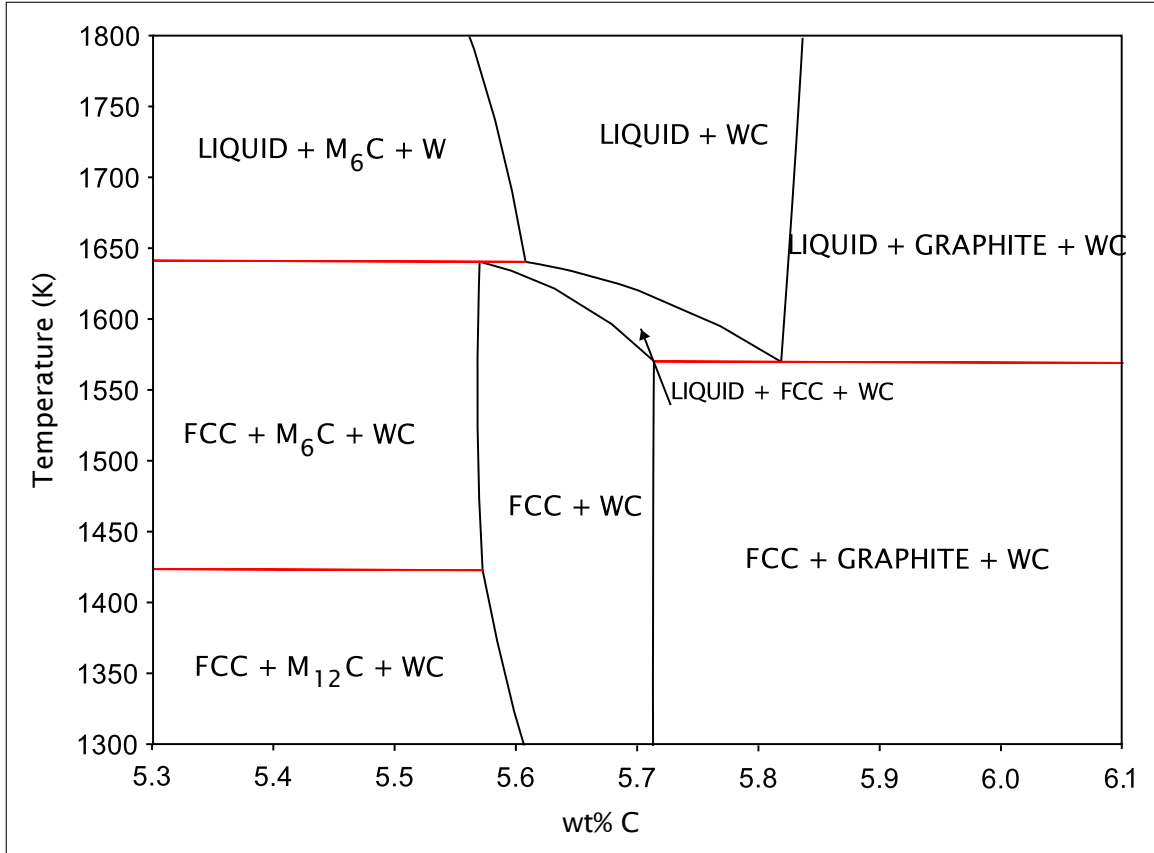


Figure 2: The calculated WC-10vol%Co phase diagram. Carbon content at which FCC+WC is present is displayed. The phase diagram was calculated using Thermo-Calc (database TCFE9).

Cobalt has become a problematic metal for several reasons, the major one being the health effects on workers in the cobalt mining and cobalt powder milling industries, especially in the Congo where more than 50% of the worlds cobalt is produced [11]. There are also concerns regarding the use of child labor and extremely poor conditions [2]. In a study by Marlies De Boeck *et al.* [1], it was concluded that Co(II) ions are genotoxic and carcinogenic in rodents. They also concluded that

there exists a link between occupational exposure to WC-Co hard metal dust and an increased risk of pulmonary cancer and that the particles are genotoxic in lung cells.

As concerns are being raised regarding the problems associated with cobalt, five cobalt salts are under investigation by the European Chemicals Agency (ECHA) to be classified as carcinogenic [12]. A regulation on the cobalt import in the EU could have a great effect on the cemented carbide industry, necessitating the development of new binder materials.

2.2.2 Alternative binders

The replacement of cobalt as binder in cemented carbides has been of interest since the development of the first cemented carbide, mainly to increase the mechanical properties. It was proposed that Fe-Ni-Co alloys are the most likely candidates [4]. Both iron and nickel are next to cobalt in the periodic table, displaying many physical similarities as described in table 1.

Several studies have been carried out investigating the possible use of Fe-Ni and Fe-Ni-Co alloys [3,4,13] as binder in cemented carbides. In a study by Chunxin Liu [3], samples of cemented carbides with 10, 15 and 20 vol% binder and a medium grain size (1.4-2.0 μm) were tested for hardness and fracture toughness. The binder materials used in the investigation were Fe-Ni alloys with varying compositions and a 70Fe-18Ni-12Co binder. The results showed that the WC-Fe-Ni-Co sample had a higher hardness and a similar fracture toughness as that of a WC-Co reference sample. One of the WC-Fe-Ni sample also had similar properties. Figure 3 shows a section of the calculated Fe-Ni phase diagram.

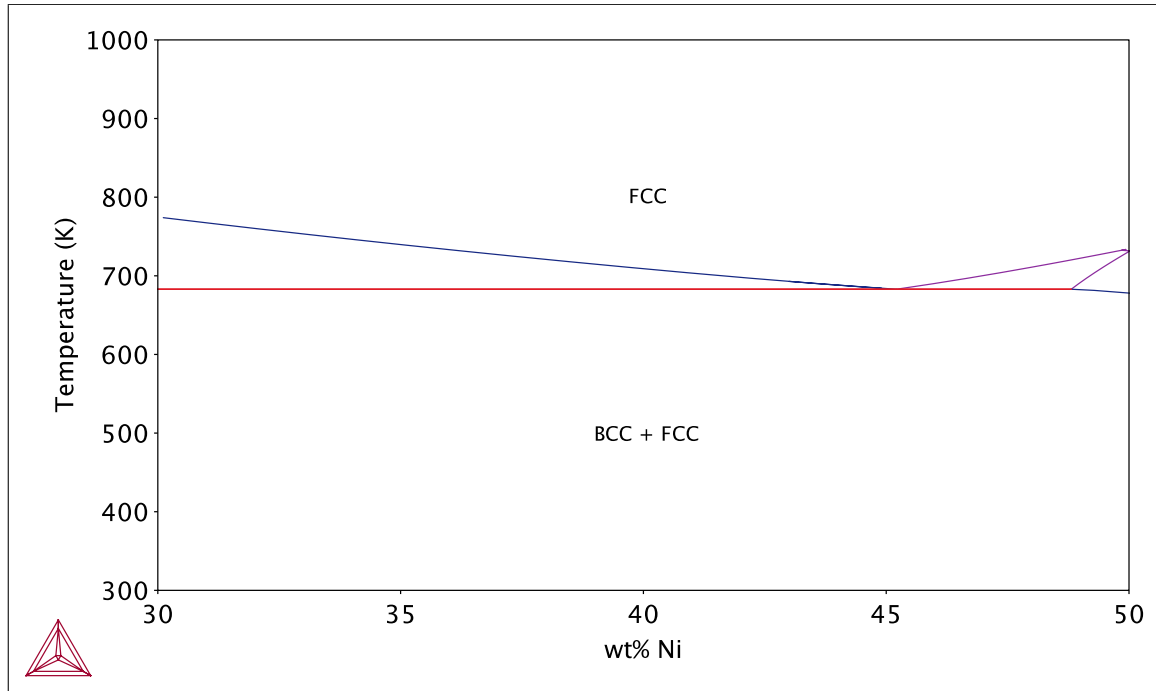


Figure 3: Section of the calculated Fe-Ni phase diagram. The phase diagram was calculated using Thermo-Calc (database TCFE9).

Table 1: Comparison between the elements Fe, Ni and Co [14].

| Element | Mass(u) | Density(g cm^{-3}) | Melting point(K) |
|---------|---------|-------------------------------|------------------|
| Fe | 55.85 | 7.87 | 1811 |
| Co | 58.93 | 8.90 | 1768 |
| Ni | 58.69 | 8.91 | 1728 |

2.3 Fracture toughness

Fracture toughness is a material property that describes a materials ability to resist fracture when a stress is applied and a crack is present [14]. The critical plane strain intensity factor K_{Ic} (MPa m^{1/2}) is used to determine the fracture toughness. In order for a fracture to occur, a crack has to be initiated [15]. When measuring the K_{Ic} , for example using the three-point Charpy-V bending method, a notch with a specific geometry is introduced to the edge of a sample with specific dimensions. The property can then somewhat accurately be reproduced and measured [9].

The fracture toughness of a material is a very complex property that involves a large number of different mechanisms that interact, most of which are still very complicated to simulate even with the most advanced methods. A few of the most common methods for modeling the fracture toughness are presented in section 3.

2.3.1 Fracture in bulk alloys

When a material is not predisposed to a specific kind of fracture, the cracks can arise and propagate in a number of different ways and directions. The most common initiation sites are at areas containing heterogeneities, often around particles or inclusions. The crack behavior inside a material strongly depends on the fraction and size of the particles that it contains. When a stress is applied, particles tend to fall out of place [16], leaving behind voids through which cracks can propagate.

In an article by Tvergaard and Hutchinson [17], it was shown that there are two mechanisms that govern the ductile fracture in a material: void-by-void or multiple void growth and coalescence. If the distance between voids x_0 is large, void-by-void growth will be the dominating mechanism. On the contrary, a smaller distance between the voids increases the likelihood of multiple void growth as described in figure 4. The K_{Ic} will decrease as multiple void growth becomes the dominating mechanism. The distance between voids can be altered by changing the void fraction and size.

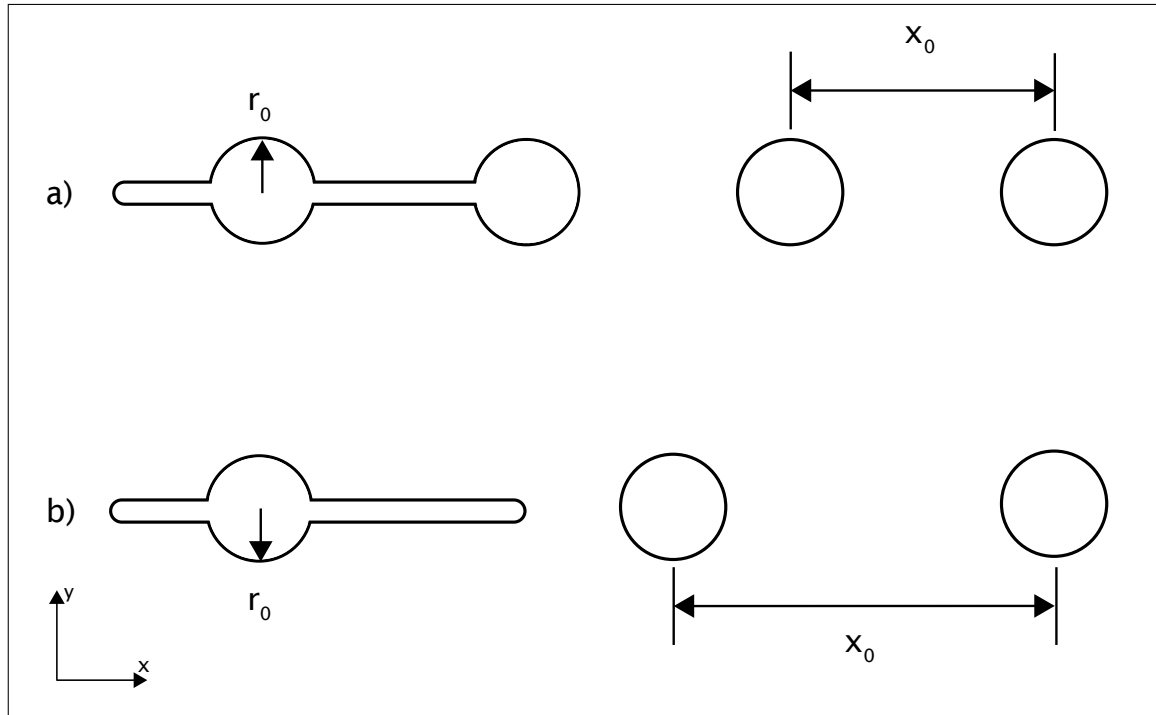


Figure 4: 2-D illustration of a crack propagating through spherical voids with radius r_0 and spacing x_0 . a)large fraction of voids, multiple void growth b)small fraction of voids, single void growth.

2.3.2 Fracture in cemented carbides

In many materials, the fracture toughness is a product of the materials ability to reduce the cracks local driving force by microstructural factors [18]. The unusually high fracture toughness relative to its hardness in cemented carbides is related to the highly effective crack tip shielding that takes place [15]. Cracks that propagate through the binder are deflected by carbide grains, effectively increasing the fracture toughness. Although the binder is a ductile phase, the fracture in cemented carbides is of brittle nature since typically 80-90 vol% of the material consists of the carbide phase. There are four major types of fracture in cemented carbides [19]:

- Transgranular binder fracture (B)
- Transgranular carbide fracture (C)
- Interfacial binder/carbide fracture (B/C)
- Intergranular carbide/carbide fracture (C/C)

B/C fracture describes the rupture in the boundary layer between carbide grains and the binder. How well the carbides are cemented to the binder is an important factor for the K_{Ic} . C/C fracture is the fracture between two carbide grains, very similar to the intergranular fracture in polycrystalline WC. C fracture is simply the cleavage of carbide grains and depends solely on the fracture toughness of the carbide. B fracture is a constrained ductile fracture that takes place inside the binder. The constraint is due to the relatively high volume fraction of carbide grains surrounding the binder. The binder merely constitutes a thin film around the carbide grains. Figure 5 illustrates the different types of fracture.

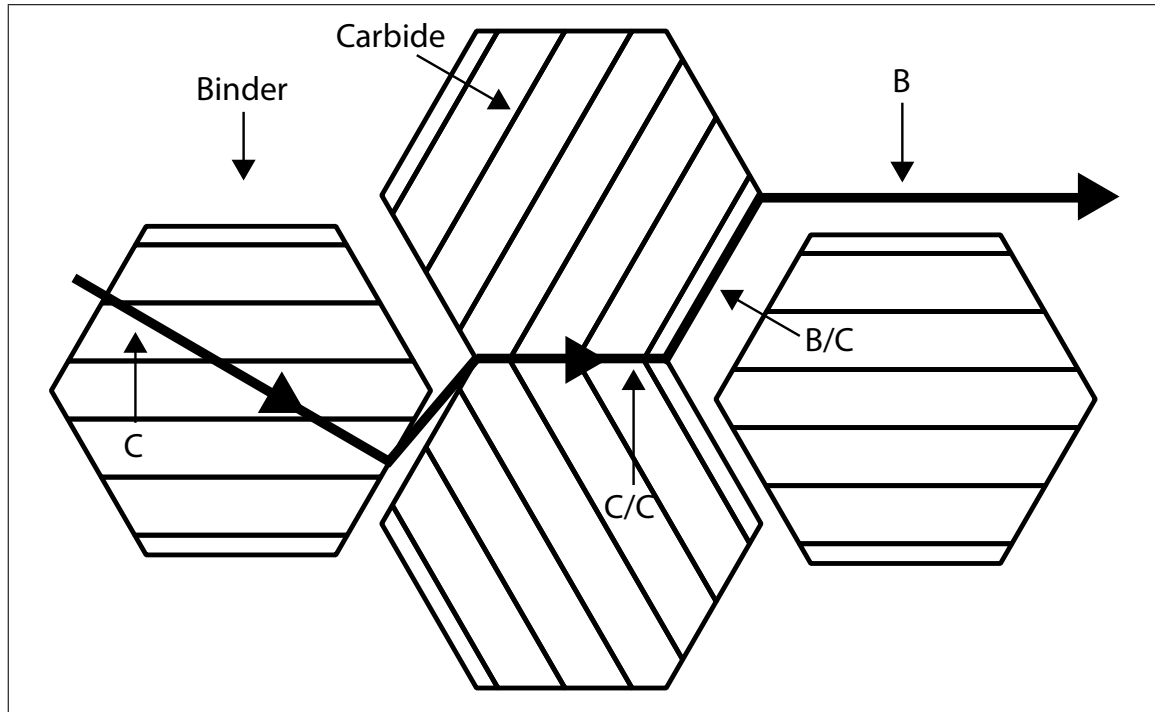


Figure 5: An illustration of the four types of fracture in a cemented carbide. The thick line describes the propagating crack. Carbide grains are striped and surrounded by the binder in white color.

2.4 Hardness

The hardness of a material is a mechanical property used to describe its resistance to localized plastic deformation, such as a dent or a scratch [14]. Thus the most common testing method of the hardness is by indentation where an indenter of a specific geometry and size is introduced into the materials surface. Depending on the indentation depth and load, a hardness number is determined. The hardness number is a relative value and defined for the specific type of testing that was performed. Conversion between different scales for hardness numbers is possible, although a comprehensive conversion scheme has yet to be developed.

There is a strong correlation between a materials hardness and its yield strength σ_y (MPa). For many metallic materials, there is an approximately proportional relationship between the two. Therefor, it is possible to convert the hardness number to a corresponding yield strength.

2.4.1 Solid solution hardening (SSH)

The hardness of a solid material can be altered by the introduction of impurities. If atoms of one element are introduced into the crystal lattice of another element, a solid solution is formed. The difference in the size of the atoms will cause a non-uniformity in the crystal lattice, impeding the motion of dislocations and thus strengthening the material [14]. Substitutional atoms occupy sites in the crystal lattice that are temporarily vacant. A substitutional atom will normally be of a similar size as the atoms of the element forming the crystal structure. Interstitial atoms inhibit normally unoccupied sites in the crystal lattice and must therefore be much smaller than the atoms forming the lattice. The effect of solid solution hardening will depend on the type of impurity atoms, as well as their quantity.

For all materials there exists a maximum limit of how many impurity atoms can occupy sites in its crystal lattice, called the solubility limit. Another important aspect is the site fraction of the atoms, denoted y . The site fraction is the fraction of the possible sites on a specific sublattice in a phase that a certain element is occupying. For FCC phases, the number of interstitial sites is the same as the number of substitutional sites [5]. Substitutional sites in a crystal lattice are denoted y' and interstitial sites y'' . Using Thermo-Calc, the solubility limit and the site fractions of elements at different temperatures can be calculated. The solid solution hardening will not only

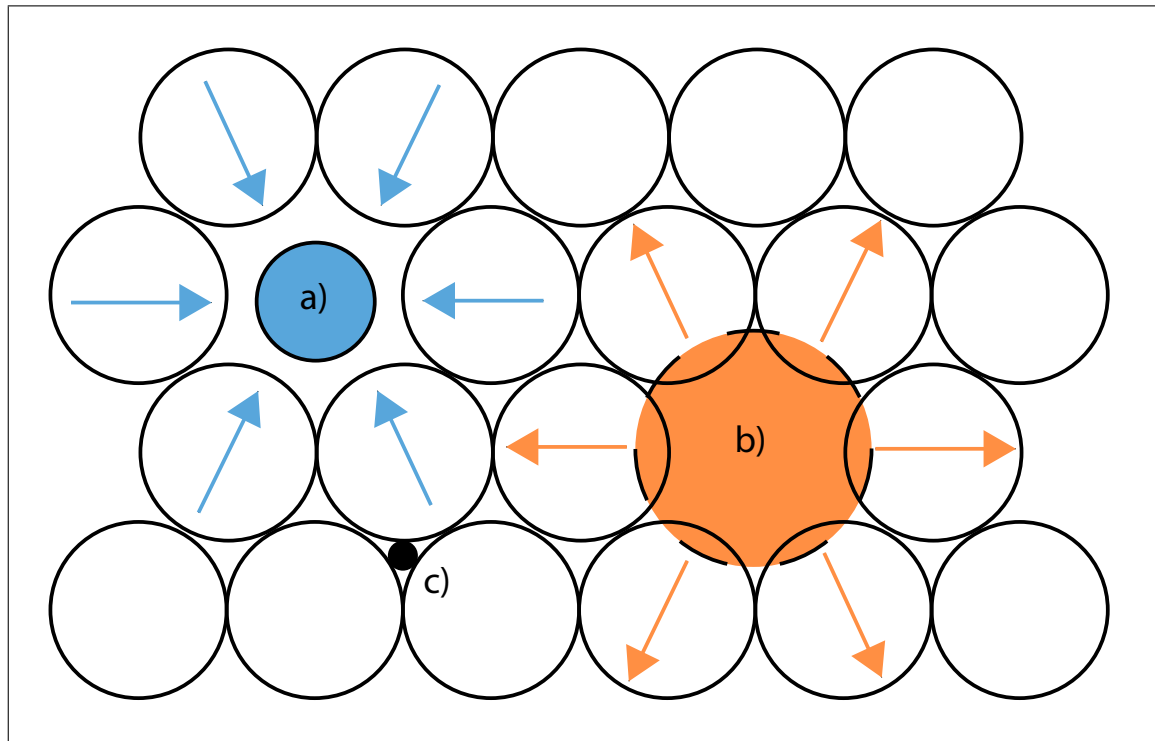


Figure 6: An illustration of the solid solution atoms in a crystal lattice. The figure shows a a)small substitutional atom, b)large substitutional atom, c)interstitial atom.

affect the hardness of a material. The fracture toughness will also be affected. An investigation by Hidetoshi Somekawa [20] on the solid solution hardening in Zn-Mn alloys showed that an increase of K_{Ic} resulted as a consequence of solid solution hardening, most likely due to the increase in yield strength.

2.4.2 Precipitation hardening

As precipitates form in a material, the dislocation motion will be affected by the disturbance in the crystal lattice caused by the incoherency between particles and the matrix [14]. For very small particles, particle cutting will be the dominating mechanism and the contribution to the strengthening will be small. As the particles grow, their ability to impede dislocations increases and the Orowan mechanism will govern the precipitates effect on the material properties. Dislocations encountering an incoherent particle will start bowing and make a loop around the particle, called Orowan looping. The described process effectively stops the dislocations movement through the matrix. Figure 7 illustrates the process of Orowan looping.

The fraction of particles is also important. A small quantity of very large particles will not be efficient at affecting the dislocations, since the probability of the dislocation to encounter the particle is small. Models for the effects of precipitation hardening have been developed for many years. The Ashby-Orowan equation is widely used for predicting the effects of particles in metallic materials [21].

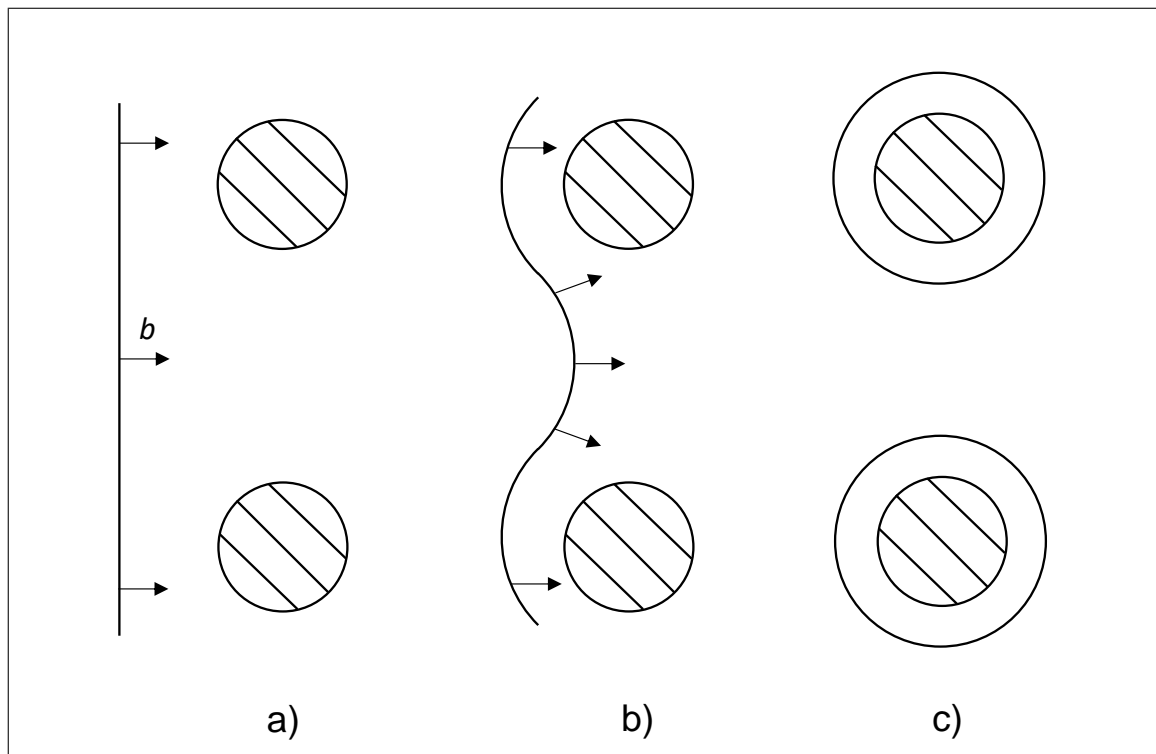


Figure 7: An illustration of Orowan looping. The figure shows a) dislocation encountering particles, b) dislocation bowing and c) dislocation forming Orowan loops around particles.

3 Method

3.1 General limitations

In order to build models for predicting the properties of bulk alloys and cemented carbides, certain approximations had to be made.

For bulk alloys, it was assumed that all cracks initiate either at sites that particles inhibit, effectively treating them as voids, or where there are pre-existing voids formed by dislocations. The particles were assumed to be perfectly spherical with a radius r_0 and evenly spaced with a distance of x_0 . The two-dimensional equivalent corresponds to cylindrical voids using the same parameters. The fraction of voids could thus be expressed as

$$f_0 = \pi \left(\frac{r_0}{x_0} \right)^2 \quad (1)$$

There was also a need for limitations on the range of f_0 and r_0 . The fraction and size of particles are manufacturing parameters that can be controlled down to very small levels. However, the cost and complexity associated with the production of such materials simply is not applicable for the production of bulk alloys and cemented carbides. Furthermore, decreasing r_0 to values below approximately 20 nm would induce the effects of particle cutting [21], which the models in this work are not designed to handle. For those reasons, this work was limited to particle fractions and sizes of $0.01 < f_0 < 0.02$ and $0.1 \mu\text{m} < r_0 < 1.0 \mu\text{m}$.

For cemented carbides, the carbide grain size d and the volume fraction of the binder V_B also needed limitations for comparability with experimental results. They were set to $0.1 < V_B < 0.2$ and $0.5 \mu\text{m} < d < 3.0 \mu\text{m}$.

The adhesion between carbide and binder was not accounted for in this work.

3.2 Computational tools

3.2.1 Softwares and databases

The tools that were used are MATLAB® [22], Thermo-Calc [23] and CES Edupack [24]. MATLAB® is a program used mainly for mathematical and technical calculations. It offers the advantage of easy and fast calculations of large amounts of data together with visual presentation of the same. MATLAB® was used to run necessary calculations and plot data.

Thermo-Calc is a software which allows the user to predict a wide variety of material properties. Most interesting for this work was to use Thermo-Calc to find equilibrium compositions of the investigated systems. The software was also used for a number of other purposes, such as finding site fractions of specific elements and amounts of phases.

CES Edupack is a database that provides empirical values of properties for elements, materials and alloys. A large number of data sheets for alloys of varying compositions is available. All of the data for G , σ_0 , ν , H and K_{Ic} used in this work were collected from the database.

3.2.2 Finite Element Method (FEM)

The Finite Element Method is a numerical method of solving problems of engineering and mathematical nature. By creating a set of finite elements, a large problem is subdivided into smaller problems that are normally simpler to handle. After rendering a set of algebraic expressions, the method can approximate necessary boundary conditions. FEM has been used in several studies on the properties of cemented carbides and binders [15, 25, 26]. The ductile fracture of void growth and coalescence can depending on the application be treated either through explicit [17] or implicit [27] modeling. FEM indentation simulates the indentation methods normally used experimentally to find the hardness H of a material.

3.3 Hardness model

3.3.1 Bulk alloy hardness

Data from FEM indentation [28] provided values of H that had been normalized on the yield strength σ_y . The data was available as a function of the Young's modulus E normalized on the yield strength σ_y as described in figure 8. Data was provided for values of the strain hardening exponent $n = 0.0, 0.1, 0.2, 0.3$.

Using MATLAB®, the data was interpolated with a model on the form

$$\left(\frac{H}{\sigma_y}\right) = a \left(\frac{E}{\sigma_y}\right)^b + c \quad (2)$$

where each set of the coefficients a, b, c is unique for each value of n as described in the appendix of this report. Figure 8 shows the available data points together with the interpolated values.

The Young's modulus of the material can be calculated using the relation

$$E = 2G(1 + \nu) \quad (3)$$

where G is the materials shear modulus and ν is the Poisson's ratio. This model provides a method for calculating the quantity H/σ_y using empirical data for G , ν and n .

A distinction between the use of the yield strength σ_y and the intrinsic yield strength σ_0 is appropriate. The intrinsic yield strength σ_0 is a hypothetical yield strength which assumes that there is no strengthening from solid solution atoms and that the material is free from particles and inclusions [5]. Thus the relation between the yield strength and the intrinsic yield strength is

$$\sigma_y = \sigma_0 + \Delta\sigma_p + \Delta\sigma_s \quad (4)$$

where $\Delta\sigma_p$ and $\Delta\sigma_s$ are the contributions from precipitation hardening and solid solution hardening respectively.

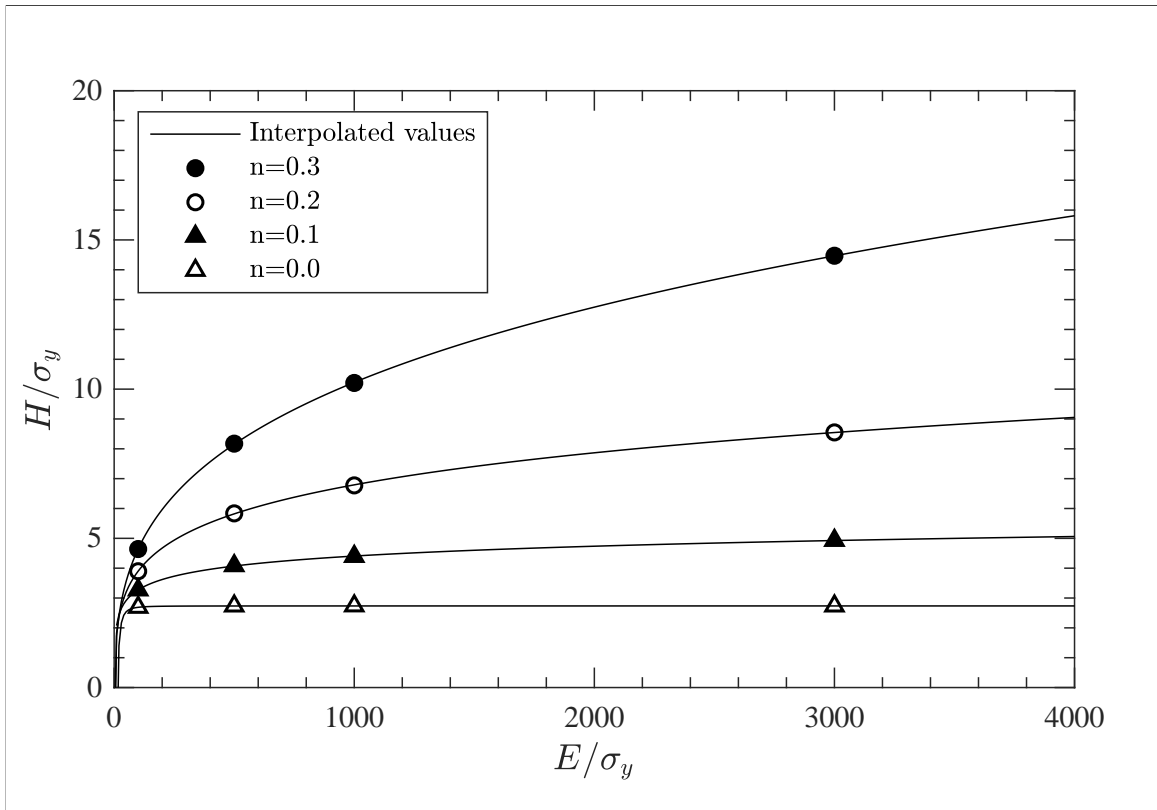


Figure 8: FEM-indentation data [28] fitted with MATLAB®. The figure shows the relationship between H/σ_y and the strain hardening exponent n as a function of E/σ_y .

3.3.2 Cemented carbide hardness

A model predicting the hardness of cemented carbides was presented in the Ph.D. thesis by Martin Walbrühl [7]. The model is based on the Enqvist model [29] which relates the cemented carbide composite hardness to the hardening range factor k , the mean free path λ and the hardness of cobalt H_{Co} and tungsten carbide H_{WC} . The model has the form

$$H_{CC} = (H_{WC} - H_{Co}) \exp\left(-\frac{k}{\lambda} + H_{Co}\right) \quad (5)$$

Where the hardness of the binder and carbide phases are in situ values. The mean free path λ of a cemented carbide is defined as the average distance between carbide grains. It is a function of the average grain size d and the volume fraction V_{Co} of the cobalt binder and can be approximated as [7]

$$\lambda = \frac{dV_{Co}}{1 - V_{Co}} \quad (6)$$

According to the same source, the tungsten carbide in situ hardness H_{WC} has been experimentally shown to follow the expression

$$H_{WC} = 693 + 2680 \cdot (2.1 + d)^{-1/2} \quad (7)$$

The model was developed for classical cemented carbides consisting of a cobalt binder phase and tungsten carbide phase. For WC-Co cemented carbides, the value of k has been determined experimentally to be approximately $35 \mu\text{m}$.

By using MATLAB®, the presented models were tested with different grain sizes and binder volume fractions. An in situ hardness of 8091 MPa [29] was used. For carbide grains, equation (7) was used for different grain sizes to model the in situ hardness.

3.3.3 Solid solution hardening model

A model predicting the strengthening from solid solution atoms was implemented to the hardness model. The model that was used was based on an article by Martin Walbrühl *et al.* [5] where the effect of solid solution atoms in a multicomponent system was studied. It is based on an equation on the form

$$\Delta\sigma_s = \left[\sum_{i=1}^N \sum_{k>j}^N A_{M_i M_k V_a} \exp\left(\frac{Q_{ik}}{RT}\right) (y'_{M_i} y'_{M_k})^{\frac{2}{3}} y''_{V_a} + \sum_{i=1}^N \sum_{j=1}^n A_{M_i I_j V_a} \exp\left(\frac{Q_{ij}}{RT}\right) (y''_{V_a} y''_j)^{\frac{2}{3}} y'_{M_i} \right] \quad (8)$$

where the summation is done over N substitutional and n interstitial elements. The model assumes binary atom interactions and its was shown to have an accuracy of 13% compared to experimental data. If the solid solution hardening of the system that is being investigated takes place in several phases, the model must be weighted for the fraction of each individual phase. A and Q are constants that vary depending on the interacting atoms and can be found in the appendix of the same article.

3.3.4 Bulk alloy precipitation hardening model

The presence of precipitates can have an effect on the materials yield strength. In order to more accurately predict the yield strength, a precipitation hardening model was implemented to the hardness model from section 3.3.1. The model that was used for the precipitation hardening contribution is based on the Ashby-Orowan's equation [21] which can be expressed as

$$\Delta\sigma_p = 0.269 \frac{Gb f_0^{1/2}}{r_0} \ln\left(\frac{r_0}{b}\right) \quad (10)$$

where b is the Burger's vector of the matrix. The assumption was made that the Young's modulus is not affected by the contribution of precipitation hardening. Figure 9 shows the effect of precipitation hardening for three different particle sizes according to the implemented model.

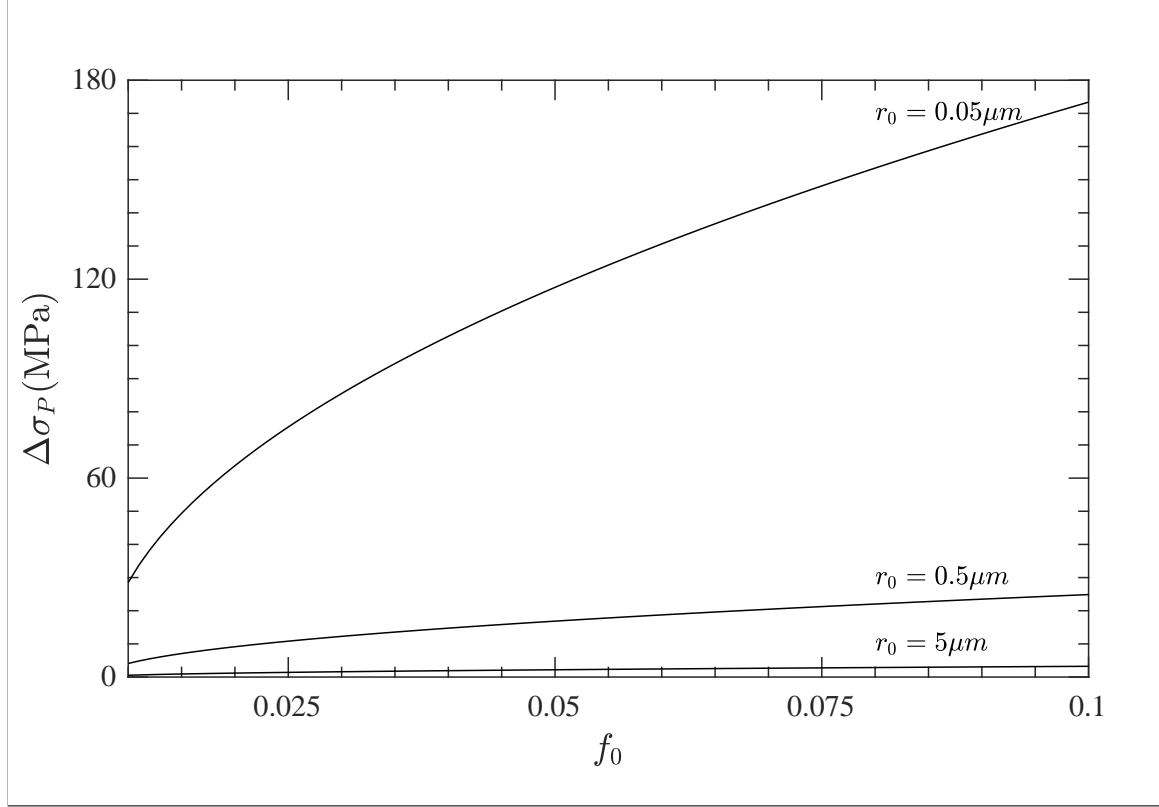


Figure 9: Effect on the yield strength from precipitation hardening according to Ashby-Orowan's equation.

3.4 Fracture toughness model

3.4.1 Bulk alloy fracture toughness

To model the bulk alloy fracture toughness, data from FEM fracture modeling [30] was used. The FEM data was based on explicit modeling of the fracture toughness of a material as a function of void spacing and fraction. A thickness of the material much greater than the void size was assumed. The data provided values of K_{Ic} that had been normalized on the yield strength σ_y and the square-root of the void spacing $\sqrt{x_0}$. The data was available as a function of the Young's modulus E normalized on the yield strength for values of the strain hardening exponent $n = 0.0, 0.1, 0.2, 0.3$ and for three different particle fractions as described in figure 10.

The data was interpolated for a continuous spectrum of fractions using MATLAB® with a model on the form

$$\left(\frac{K_{Ic}}{\sigma_y x_0^{1/2}} \right) = a (f_0)^b + c \quad (9)$$

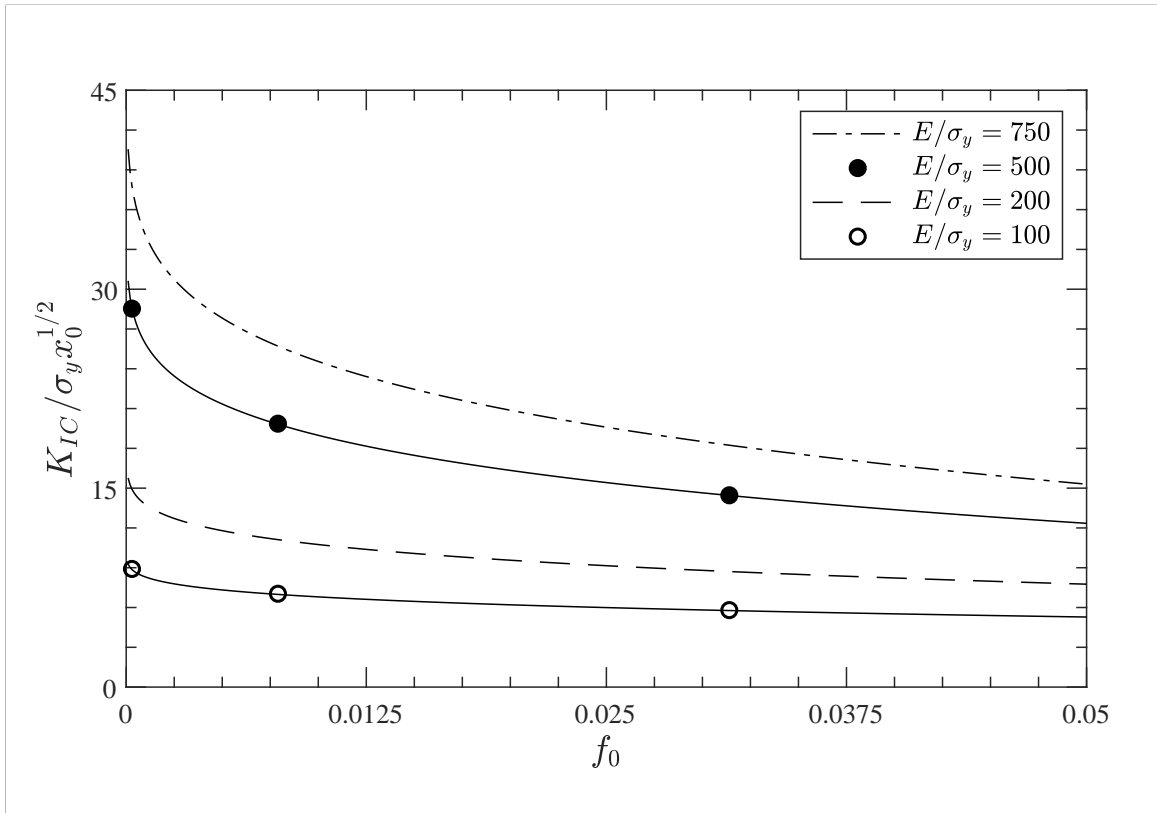


Figure 10: FEM fracture data [30] fitted with MATLAB®. The figure shows the relationship between the fracture toughness and E/σ_y for different void fractions. All values are for $n=0.0$.

The coefficients a, b, c were thus only valid for the specific values of E/σ_y given by the data as described in the appendix of this report. Spline interpolation was used to approximate the coefficients for any value of E/σ_y . Figure 10 shows interpolated function values for the given data together with functions with interpolated coefficients. All values in the figure are assuming a strain hardening exponent of 0.0.

The square-root of the distance between voids can according to (1) be expressed as

$$x_0^{1/2} = \pi^{1/4} \frac{r_0^{1/2}}{f_0^{1/4}}$$

Combining the described model with empirical values of σ_y , the K_{Ic} of a material can be approximated for any predetermined void volume fraction and radius.

3.4.2 Cemented carbide fracture toughness

For the modeling of the K_{Ic} of cemented carbides, a slightly different approach from that of bulk alloys had to be used. In cemented carbides, the fracture mechanisms depend on four different types of fracture as described in section 2. Since the fracture toughness of a cemented carbide will depend on the fracture behavior displayed by each of the four types of fracture, the term strain energy release rate G' which describes the energy required for each fracture type to occur is introduced. The notation G' for strain energy release rate is used to avoid confusion with the shear stress G . It is directly related to the fracture toughness of a material. Each of the fracture types will have their independent energy release rate [13]. For this report, the simplification was made that $G'_{C/C} \approx G'_C$ and $G'_{C/B} \approx G'_B$. This assumption is based on the fact the C and C/C types of fracture are very closely related, and that the B and C/B types are more related to constrained deformation than to the actual boundary adhesion. The area fraction A is introduced since the strain release energy is dependent on the newly created surface area. Each of the contributions to the strain energy release rate can thus be weighted by its individual area fraction.

The model used to predict the K_{Ic} of cemented carbides has the form [9]

$$K_{Ic} = \left(\frac{E_{CC}}{1 - \nu_{CC}^2} (A_C G'_C + A_B G'_B) \right)^{1/2} \quad (11)$$

where E_{CC} and ν_{CC} are the Young's modulus and Poisson's ratio of the cemented carbide respectively. G'_C and G'_B are the energy release rates for the carbide phase and the binder phase respectively and can be approximated using the relation [31]

$$G'_{IC} = \frac{K_{Ic}^2}{E(1 - \nu^2)} \quad (12)$$

An article by H.E. Exner [13] covering the fracture mechanisms in cemented carbides presented a method of approximating the surface fraction related to different kinds of fracture in cemented carbides. The area fraction can be approximated using the relations

$$A_C = \frac{d}{0.4d + 3.1} \exp(-1.77V_B^{0.78}) \quad (13)$$

$$A_B = \frac{d}{1.5d + 1.1} (1 - \exp(-1.77V_B^{0.78})) \quad (14)$$

FEM data [32] was used to predict the energy release rate of the binder G'_B . The data was fitted in a similar manner as described in section 3.4.1. The main difference between the approaches are that FEM fracture modeling for binders in cemented carbides are done by assuming a film of the binder with limited thickness [32]. This accounts for the fact that inside a cemented carbide, the binder exists as layers between the carbide grains, thus being constrained to a certain thickness h [13]. The results produced from FEM modeling will be affected by modeling a different thickness of the binder. Generally, a decrease in binder thickness leads to lower values of the fracture toughness and less sensitivity to void fraction. Figure 11 shows the K_{Ic} normalized on the yield strength and the square root of particle spacing for binders of different thickness. h refers to the thickness of the material which is related to the void spacing. Bulk refers to a material where the thickness is much greater than the void spacing. The modeled values are for a material with the properties $n = 0.2$ and $E/\sigma_y = 500$. Coefficients for the fitted model are presented in appendix A.

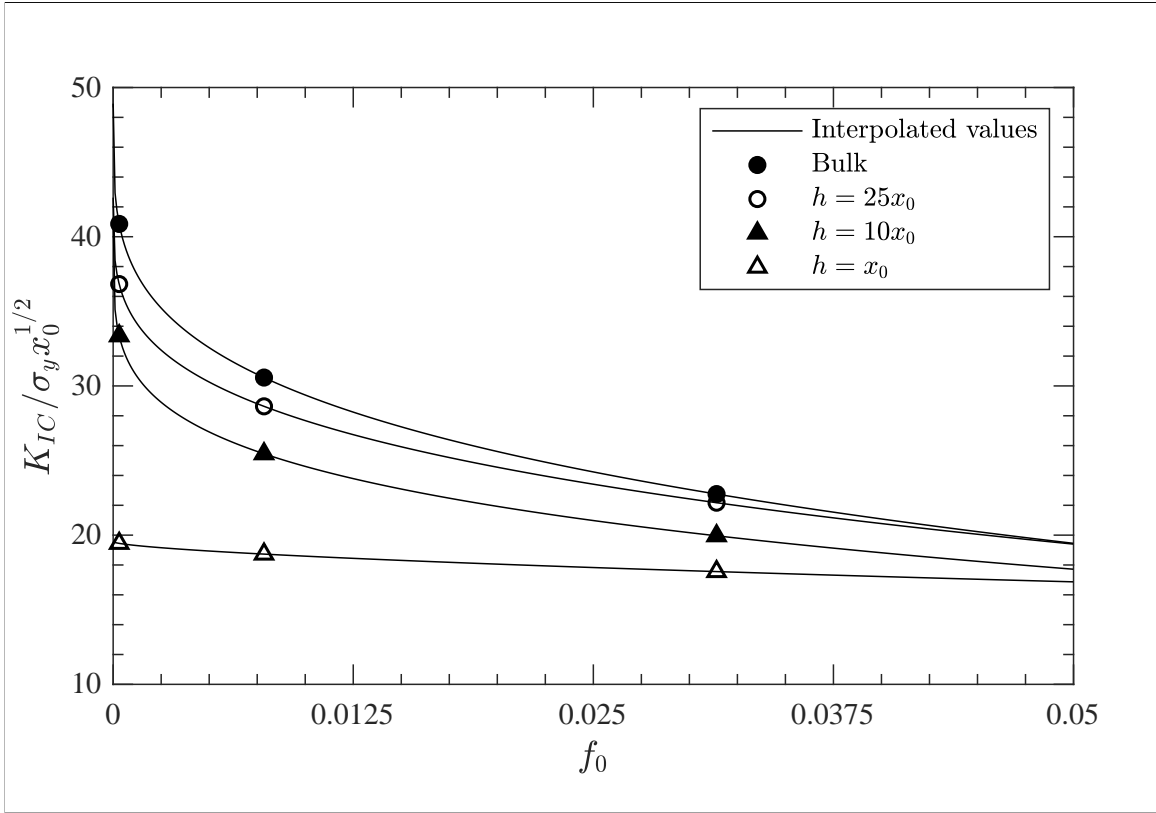


Figure 11: FEM fracture data [32] for materials of different thickness fitted with MATLAB[®]. All values are for a material with properties $n = 0.2$ and $E/\sigma_y = 500$.

3.5 Optimizing material properties

The use of MATLAB[®] allows for combining the different models, providing a tool for optimizing the material properties. Since both hardness and fracture toughness are important properties, it is not sufficient to study them independently. An optimization is necessary in order to find the best possible combination of properties exhibited by the material.

There are a number of different methods that could be used for optimizing the K_{Ic} and H of a material. In this work, the optimization that was used was simply multiplying the values of each of the individual properties, yielding an optimization function

$$F = H \cdot K_{Ic} \quad (15)$$

Although the function F ($\text{MPa}^2 \text{m}^{1/2}$) does not have any significance in a strictly physical sense, it is an efficient way of determining whether the material fulfills certain parameters without having to study them independently. The inverse relation between hardness and fracture toughness is well-known and widely accepted. Thus the goal of optimization is to improve the combination of the properties.

4 Results

4.1 Fracture toughness model verification

An article by L. Beuvineau *et al.* [33] investigating the effects of f_0 and x_0 on the fracture initiation toughness J_{IC} of a C-Mn steel was used to verify the model presented in section 3.4.1. In the report, a piece of steel of composition 98.8Fe/1Mn/0.2C by weight percent was rolled and cut in the transverse longitudinal and the longitudinal short directions. The size of and average distance between particles was approximated. Particles were either oblate or prolate and were defined by the initial aspect ratio $W_0 = r_y/r_x$ as described in figure 12. The larger the value of W_0 the more prolate of a particle and vice versa. An estimation of f_0 was 0.0025. It included experimentally measured values of the fracture initiation toughness J_{IC} . The material was characterized by $\sigma_0 = 190$ MPa and $n = 0.27$. Table values of similar steels were used to estimate the mechanical properties of $G = 80\,000$ GPa and $\nu = 0.3$ [34]. The relationship between $J_{IC} = (1 - \nu^2)K_{Ic}^2 E$ [17] was used for conversion purposes. An article by Tvergaard and Hutchinson [17] provided a graph describing $J_{IC}/x_0\sigma_0$ as a function of f_0 for prolate, spherical and oblate particles. It revealed a reduction in $J_{IC}/x_0\sigma_0$ by approximately 15% from prolate to spherical particles and an increase by approximately 20% from oblate to spherical particles. Thus, fracture toughness will be lower for materials containing oblate particles than those with prolate particles.

An attempt was made to verify the bulk alloy fracture toughness model using the results from the study. First, the fracture initiation toughness J_{IC} values were converted to fracture toughness K_{Ic} . For both types of voids, the crack propagates in the x-direction. For simplicity, spherical voids with radius r_y were assumed. For the prolate void, r_y was estimated using equation (1) to be 2.34 μm . For the oblate particles, r_x was calculated to be 5.04 μm . Since the particles were oblate and $W_0 = 0.13$, r_y was calculated to be 0.66 μm . The results are presented in table 2. Experimental values were converted to equivalent spherical particle values and added for comparison.

Table 2: Experimental and predicted K_{Ic} values for prolate and oblate particles using the bulk alloy fracture toughness model.

| f_0 | $x_0(\mu\text{m})$ | W_0 | $r_0(\mu\text{m})$ | $K_{Ic}(\text{exp.})(\text{MPa})$ | $K_{Ic}(\text{pred.})(\text{MPa})$ |
|--------|--------------------|-------|--------------------|-----------------------------------|------------------------------------|
| 0.0025 | 83 | 1.7 | 2.34 | 136 | 151 |
| 0.0025 | 179 | 0.13 | 0.66 | 118 | 107 |

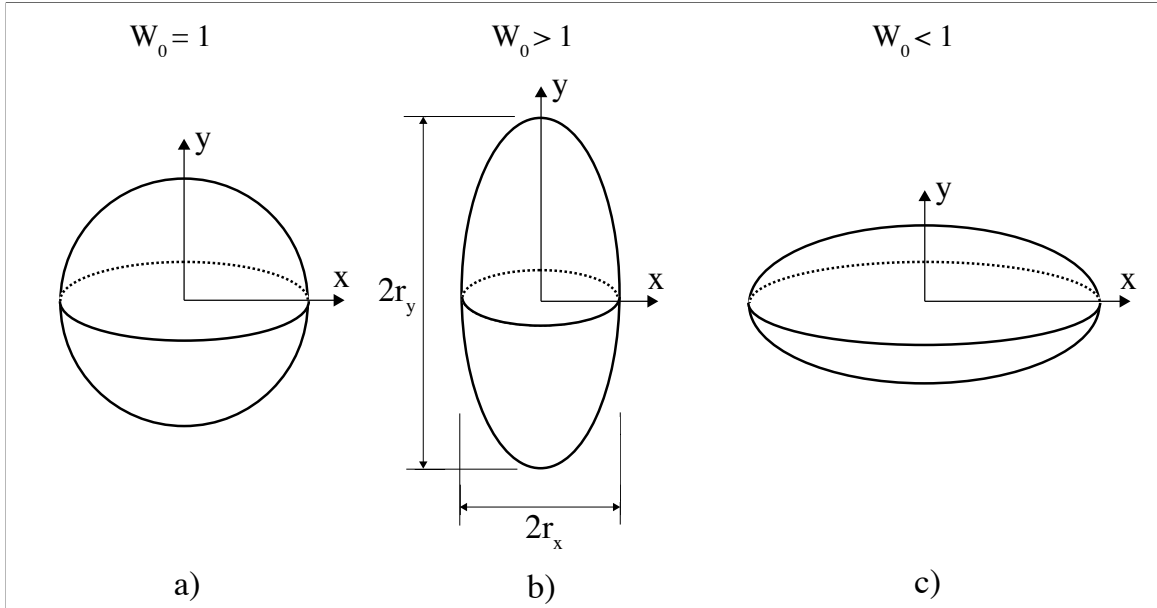


Figure 12: Illustration of the geometry of a)spherical, b)prolate, c)oblate particles. Cracks propagate in the x-direction.

4.2 Bulk alloys

For the investigation of the mechanical properties of bulk alloys, several different materials in the Fe-Ni system with different compositions as described in table 3 were chosen. All of the empirical data for the properties of the materials was gathered from CES Edupack. The different materials were labeled as #1-4 where cobalt is listed as #1 and used as a reference and for comparison. All of the materials that were investigated had according to data been annealed at 755 K which facilitated the comparison, since they were assumed to have similar microstructures. The material treatments and types are summarized in table 4 together with other relevant properties. Figure 8 was used to estimate the strain hardening exponent for each of the materials. For Fe-Ni alloys, a Burger's vector of 0.25 nm was used. For pure cobalt, it was set to 0.17 nm.

For material #1, it was assumed that no solid solution hardening takes place since it is a pure element. For materials #2-3, it was assumed that the solid solution hardening between Fe and Ni atoms is already accounted for in the empirical data used for σ_0 . Thus for materials #1-3, it was assumed that the relation $\sigma_y = \sigma_0 + \Delta\sigma_p$ is valid. Any effects from solid solution are included in σ_0 .

For material #4, an attempt was made to test the solid solution hardening model in a Fe-Ni alloy. Titanium (Ti) and carbon was added using Thermo-Calc and the effects of solid solution hardening were simulated using the described model. Results showed that the present phases were FCC+TiC with a ratio of approximately 60vol% FCC and 40vol% TiC. The composition of the FCC phase of material #4 was approximately the same as material #2, so the same σ_0 was used. Thus for material #4, the relationship $\sigma_y = \sigma_0 + \Delta\sigma_s + \Delta\sigma_p$ was applied. Detailed descriptions of the alloys and the use of the solid solution hardening model are presented under the individual subsections of this report.

Table 3: Mechanical properties and compositions [34] of the materials chosen for modeling and optimization.

| # | Fe(wt%) | Ni(wt%) | Co(wt%) | Misc.(wt%) | σ_y (MPa) | E(GPa) | G(GPa) | ν |
|---|---------|---------|---------|------------|------------------|--------|--------|-------|
| 1 | 0 | 0 | 99.3 | 1> | 485 | 218 | 84 | 0.3 |
| 2 | 50-57 | 44-46 | 0 | 1> | 245 | 221 | 85 | 0.3 |
| 3 | 62-65 | 35-37 | 0 | 1> | 315 | 151 | 58 | 0.3 |
| 4 | 56 | 44 | 0 | 1> | 272 | 221 | 85 | 0.3 |

Table 4: Additional information on the chosen materials. Values marked with + are estimates.

| # | Type | Treatment | E/σ_y | H (MPa) | K_{Ic} (MPa m ^{1/2}) | n |
|---|---------|-----------|--------------|-----------|----------------------------------|-----|
| 1 | Pure Co | Annealed | 450 | 1961 | 150 ⁺ | 0.1 |
| 2 | 45Ni/Fe | Annealed | 902 | 1373 | 239 ⁺ | 0.2 |
| 3 | Invar | Annealed | 479 | 1765 | 239 ⁺ | 0.2 |
| 4 | 43Ni/Fe | Annealed | 813 | N/A | N/A | 0.2 |

4.2.1 Material #1: Pure cobalt

Cobalt of 99.3% purity was added for comparison with the bulk alloys. The cobalt had been annealed at a temperature of approximately 755 K. The high temperature phase of cobalt is FCC. An equilibrium transformation to the room temperature HCP structure takes place at approximately 700 K. Figure 13 shows contour plots of the values of F for different void fractions and sizes. In table 5, the maximum and minimum values of $F(H \cdot K_{Ic})$ together with the corresponding H and K_{Ic} values are presented.

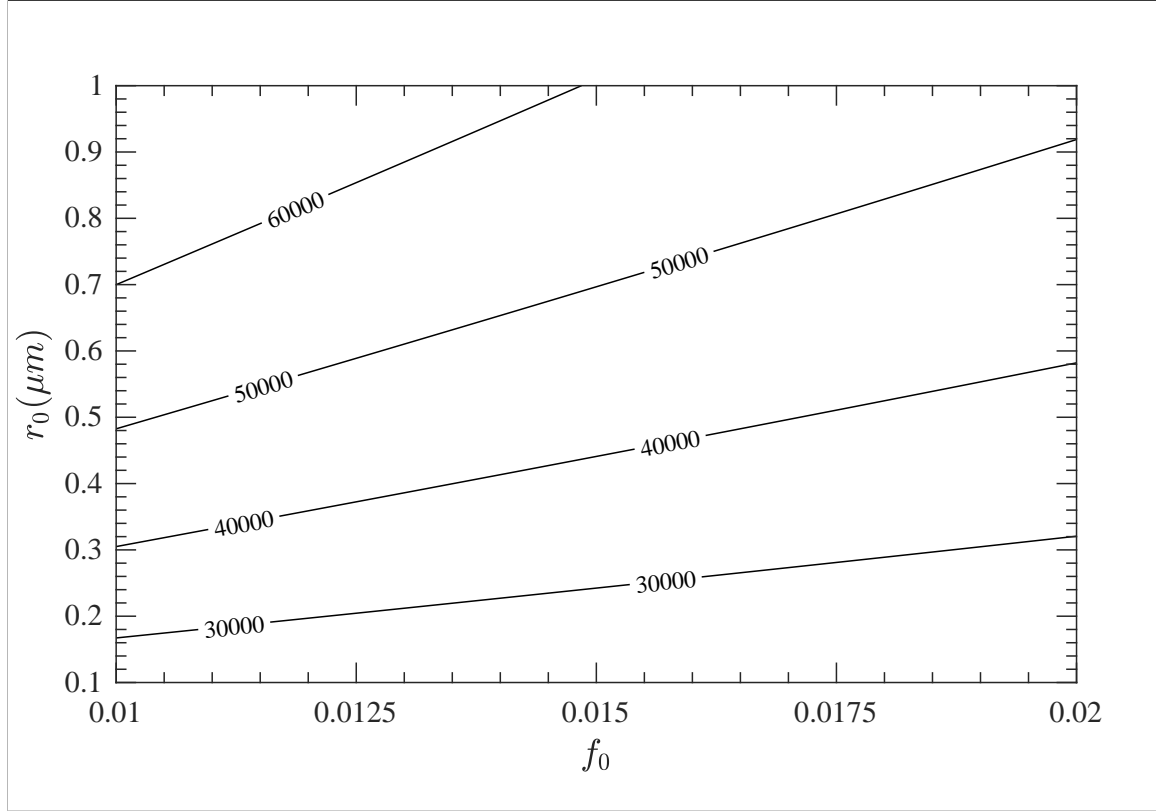


Figure 13: F values for cobalt 99.3% purity. Contour lines indicate values of $H \cdot K_{Ic}$.

Table 5: Maximum and minimum values of F with the corresponding fracture toughness and hardness values of pure cobalt.

| | $F(\text{MPa}^2 \text{m}^{1/2})$ | $K_{Ic}(\text{MPa m}^{1/2})$ | $H(\text{MPa})$ |
|---------|----------------------------------|------------------------------|-----------------|
| Maximum | 114×10^3 | 58.2 | 2093 |
| Minimum | 17.1×10^3 | 8.2 | 1957 |

4.2.2 Material #2: 45Ni/Fe

An annealed 45Ni-Fe alloy was investigated using the presented models. According to data, annealing took place at a temperature of approximately 755 K. The alloy had the highest shear modulus of all of the investigated materials. According to figure 3, the equilibrium phase at the annealing temperature is FCC. At room temperature, it is expected to be in the BCC+FCC two-phase region. The F values are shown in figure 14. In table 6, the maximum and minimum values of $F(H \cdot K_{Ic})$ together with the corresponding H and K_{Ic} values are presented.

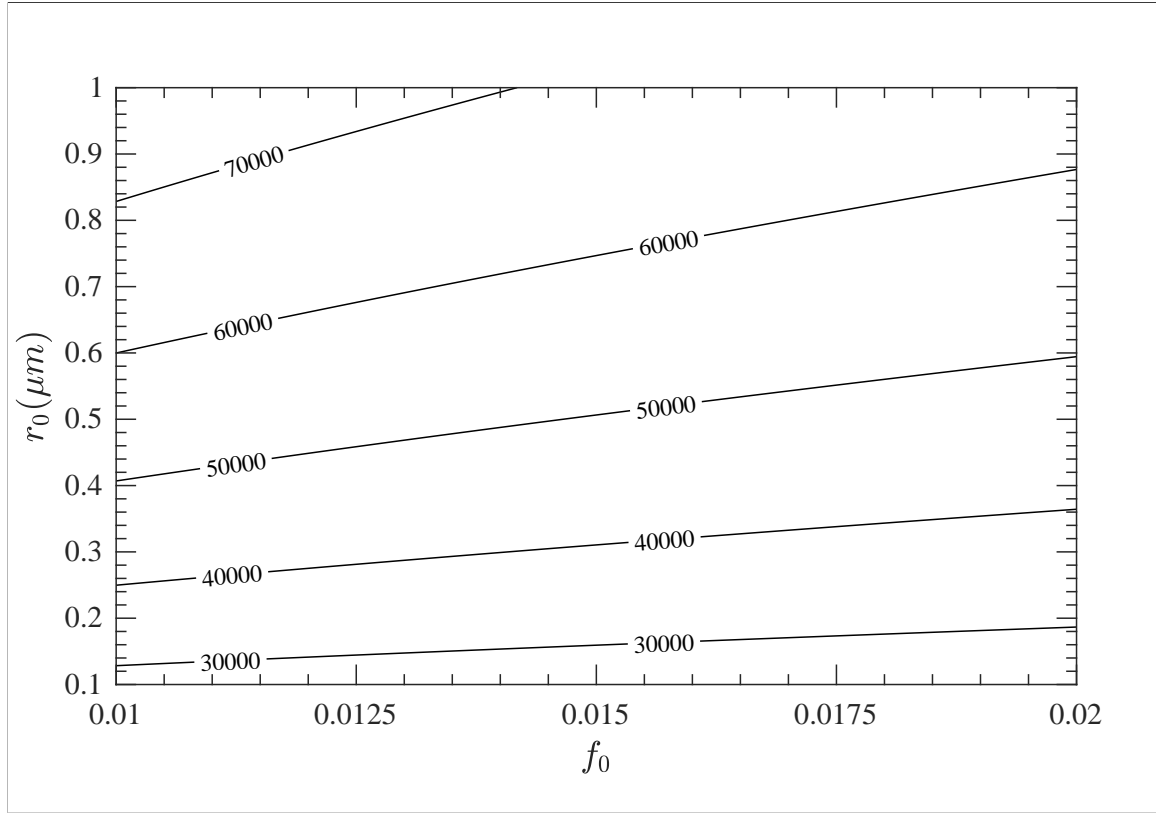


Figure 14: F values for a 45Ni/Fe bulk alloy. Contour lines indicate values of $H \cdot K_{Ic}$.

Table 6: Maximum and minimum values of F with the corresponding fracture toughness and hardness values of material #2.

| | $F(\text{MPa}^2 \text{m}^{1/2})$ | $K_{Ic}(\text{MPa m}^{1/2})$ | $H(\text{MPa})$ |
|---------|----------------------------------|------------------------------|-----------------|
| Maximum | 121×10^3 | 73.8 | 1956 |
| Minimum | 23.3×10^3 | 11.9 | 1641 |

4.2.3 Material #3: Invar alloy

An Invar alloy with the composition presented in table 3 was chosen for investigation. The alloy had been annealed at approximately 755 K. According to data the alloy had a similar fracture toughness to that of material #2. Figure 3 shows that the equilibrium phase at annealing temperature is either 100% FCC or FCC with small amounts of BCC depending on the exact composition. At room temperature, it is expected to be in the BCC+FCC two-phase region. In table 7, the maximum and minimum values of $F(H \cdot K_{Ic})$ together with the corresponding H and K_{Ic} values are presented.

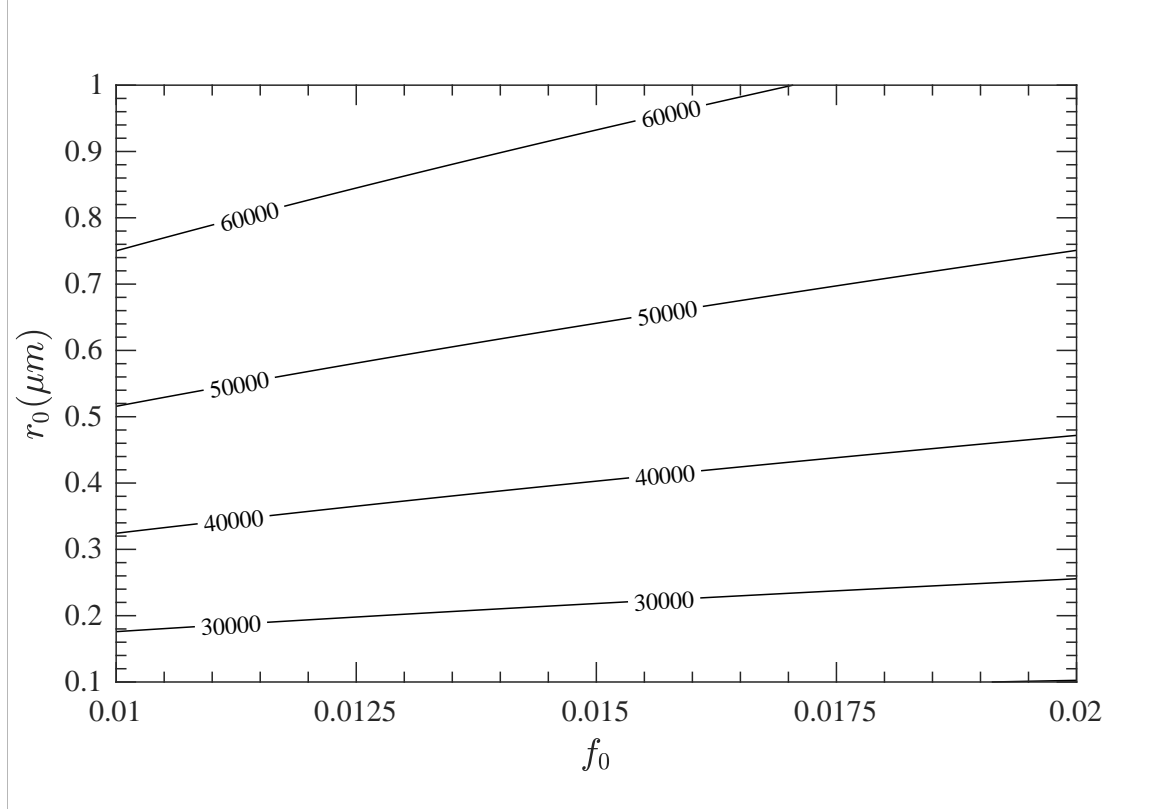


Figure 15: F values for a Invar bulk alloy. Contour lines indicate values of $H \cdot K_{Ic}$.

Table 7: Maximum and minimum values of F with the corresponding fracture toughness and hardness values of material #3.

| | $F(\text{MPa}^2 \text{m}^{1/2})$ | $K_{Ic}(\text{MPa m}^{1/2})$ | $H(\text{MPa})$ |
|---------|----------------------------------|------------------------------|-----------------|
| Maximum | 110×10^3 | 60.2 | 2009 |
| Minimum | 19.6×10^3 | 9.75 | 1822 |

4.2.4 Material #4: 45Ni/Fe with C and Ti

An attempt was made to test the solid solution hardening model in a Fe-Ni bulk alloy. Using Thermo-Calc, titanium (Ti) and carbon was added to a Fe-Ni alloy. The goal was to have a two-phase material consisting of FCC+TiC to investigate the effects of substitutional Ti atoms and interstitial C atoms in the Fe-Ni matrix. The temperature at which solution of atoms took place was chosen to be 755 K since annealing in all of the presented materials took place at said temperature. The necessary amounts of Ni and Fe to have a FCC+TiC structure at the annealing temperature were calculated and added to the Thermo-Calc calculations. The results are presented in table 8.

Values of site fractions that were used in the solid solution hardening model were collected using Thermo-Calc and are presented in table 9 together with the calculated increase in yield strength. The composition of the FCC phase was according to Thermo-Calc 44Ni/56Fe given in percentage by weight, which falls in the range of the composition of material #2. Thus it was assumed that σ_0 for material #2 could be used for material #4. Since the empirical σ_0 of material #2 already accounts for interactions between Fe and Ni atoms, they were neglected in the solid solution hardening model. Constants A and Q for the binary atom interactions were available in the article where the solid solution hardening model was presented [5].

The simulated $\Delta\sigma_s$ was added to the σ_0 of material #2 to yield a new σ_y of 272 MPa and thus $E/\sigma_y = 813$. Figure 16 shows the F values of material #4 after solid solution hardening of C and Ti atoms had been simulated. In table 10, the maximum and minimum values of $F(H \cdot K_{Ic})$ together with the corresponding H and K_{Ic} values are presented.

Table 8: Amounts of elements added to material #4 in Thermo-Calc. The amounts were calculated assuming a stoichiometric ratio of Ti and C.

| Fe (wt%) | Ni (wt%) | Ti (wt%) | C (wt%) |
|----------|----------|----------|---------|
| 40 | 30 | 19 | 11 |

Table 9: Values of site fractions used for solid solution hardening calculation and the increase in yield strength of material #4.

| y'_{Fe} | y'_{Ni} | y'_{Ti} | y''_C | y''_{Va} | $\Delta\sigma_s$ (MPa) |
|-----------|-----------|----------------------|--------------------|-------------|------------------------|
| 0.584 | 0.416 | 3.8×10^{-8} | 4×10^{-4} | ≈ 1 | 27 |

Table 10: Maximum and minimum values of F with the corresponding fracture toughness and hardness values of material #4.

| | F (MPa 2 m $^{1/2}$) | K_{Ic} (MPa m $^{1/2}$) | H (MPa) |
|---------|----------------------------|----------------------------|-----------|
| Maximum | 163×10^3 | 83.5 | 2261 |
| Minimum | 30.6×10^3 | 13.5 | 1953 |

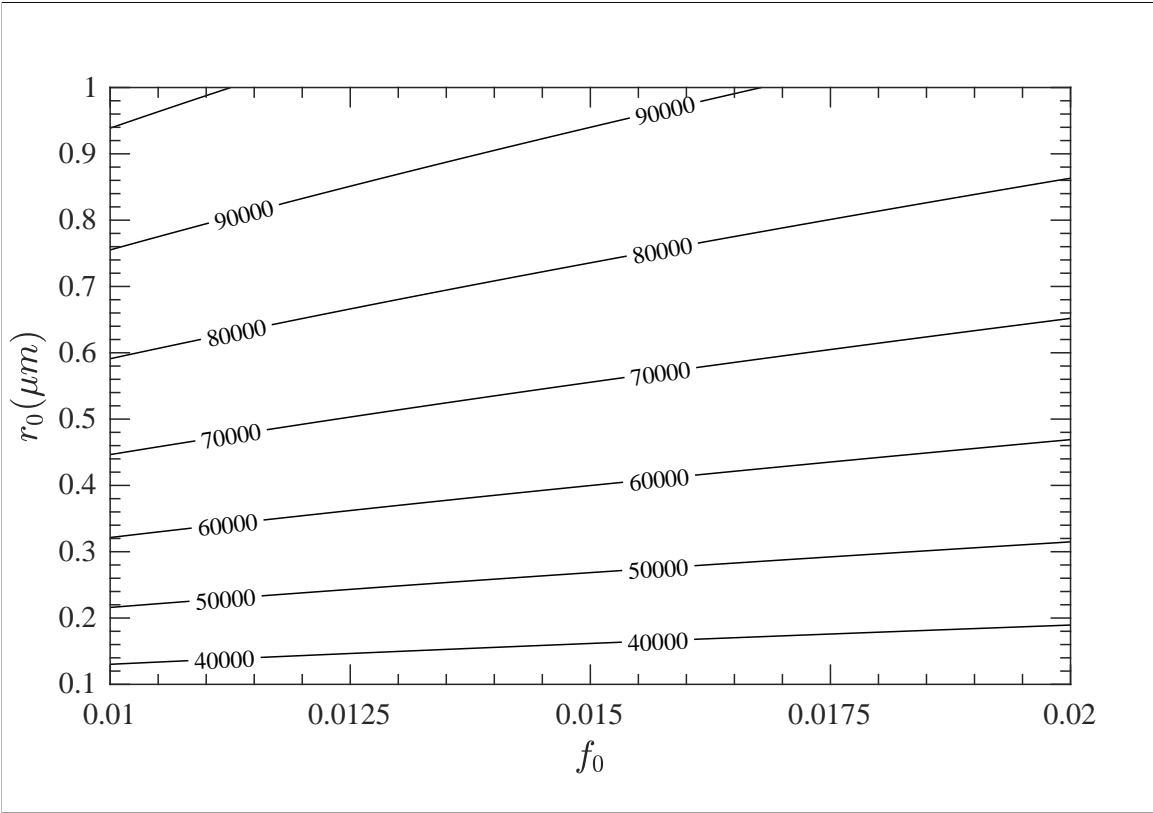


Figure 16: F values for a Invar bulk alloy with solid solution hardening. Contour lines indicate values of $H \cdot K_{Ic}$.

For easy comparison, the maximum and minimum F values for all of the materials with the corresponding H and K_{Ic} are listed and summarized in table 11. The maximum values of $H \cdot K_{Ic}$ are located where r_0 is at a maximum and f_0 is at a minimum. The maximum K_{Ic} values coincide with the maximum values of F . The maximum values of H coincide with the minimum values of F . They are found where r_0 is at a minimum and f_0 is at a maximum.

Comparing the maximum and minimum values of F show that there is a 80-85% decrease in $H \cdot K_{Ic}$ if r_0 is decreased from 1 to 0.1 μm and f_0 is increased from 0.01 to 0.02.

Table 11: Summary of the maximum and minimum values of F with the corresponding fracture toughness and hardness values of pure cobalt and the investigated alloys.

| | # | $F(\text{MPa}^2 \text{m}^{1/2})$ | $K_{Ic}(\text{MPa m}^{1/2})$ | $H(\text{MPa})$ |
|---------|---|----------------------------------|------------------------------|-----------------|
| Maximum | 1 | 114×10^3 | 58.2 | 2093 |
| | 2 | 121×10^3 | 73.8 | 1956 |
| | 3 | 110×10^3 | 60.2 | 2009 |
| | 4 | 163×10^3 | 83.5 | 2261 |
| Minimum | 1 | 17.1×10^3 | 8.20 | 1957 |
| | 2 | 23.3×10^3 | 11.9 | 1641 |
| | 3 | 19.6×10^3 | 9.75 | 1822 |
| | 4 | 30.6×10^3 | 13.5 | 1953 |

4.3 Cemented carbides

The F values of cemented carbides with a cobalt binder phase were modeled using the methods described in section 3. Since the amount of the binder in a cemented carbide is approximately 10-20 vol%, the carbide phase could be considered the matrix. As previously described, the binder is a thin film between the carbide grains and is very limited in thickness. Thus the effects of precipitation hardening in the binder phase will be negligible. Precipitates in bulk alloys are normally larger than the binder thickness in cemented carbides. Thus it was assumed that for cemented carbides $\sigma_p = 0$.

4.3.1 WC-Co cemented carbides

The solid solution hardening contribution from tungsten and carbon atoms in the cobalt binder crystal lattice was simulated using the solid solution hardening model. A sintering temperature of 1673 K was assumed and the site fractions of cobalt, tungsten and carbon atoms were calculated with Thermo-Calc. According to figure 2, the cemented carbide phases after cooling would be FCC+WC. Since the site fraction of atoms depends on the binder content [3], site fractions for cemented carbides with 10, 15 and 20 vol% Co were calculated. In table 12 the amounts of elements used for calculations of materials with different volume fractions of the binder is presented. Table 13 shows the calculated site fractions together with the increase in yield strength as a result of solid solution hardening. An average of $\Delta\sigma_s = 347.9$ was used in calculations.

Table 12: Amounts of elements added in Thermo-Calc for different binder volume contents. Calculations were made assuming a stoichiometric ratio between W and C.

| Binder(vol%) | Co (wt%) | W (wt%) | C (wt%) |
|--------------|----------|---------|---------|
| 10 | 6.99 | 87.27 | 5.74 |
| 15 | 10.66 | 83.83 | 5.51 |
| 20 | 14.46 | 80.26 | 5.28 |

Table 13: Values of site fractions used for solid solution hardening calculations and the increase in yield strength.

| Binder(vol%) | y'_{Co} | y'_W | y''_C | y''_{Va} | $\Delta\sigma_s(\text{MPa})$ |
|--------------|-----------|--------|---------|------------|------------------------------|
| 10 | 0.9955 | 0.0045 | 0.0122 | 0.985 | 348.7 |
| 15 | 0.9955 | 0.0045 | 0.0122 | 0.985 | 347.5 |
| 20 | 0.9955 | 0.0045 | 0.0123 | 0.985 | 347.5 |

The K_{Ic} of the WC-Co cemented carbide was modeled using equation (11) with values $G_{CC} = 283 \text{ GPa}$, $\nu_{CC} = 0.2$ and $G'_{CC} = 2 \times 10^{-4} \text{ MPa m}$ [34]. The G'_B of the binder had to be approximated using thin film FEM data. A volume fraction of 0.001 and radius of 0.2 μm of voids was assumed. Together with the new yield strength of the binder, equation (9) rendered an approximated in situ binder fracture toughness of $K_{Ic} = 40 \text{ MPa}$ and thus $G'_B = 0.018 \text{ MPa m}$. With all the parameters calculated or approximated, the K_{Ic} for different carbide grain sizes and binder fractions was simulated. The hardness of the cemented carbide was modeled using equation (5) for the same grain sizes and binder fractions as the fracture toughness. The contribution of the solid solution hardening was added to the binder hardness of 8091 MPa [29] to yield a total in situ hardness of 8439 MPa. The hardness of the tungsten carbide grains was modeled using equation (7).

A comparison between the simulated results and experimental ones was made. The hardness and fracture toughness of a WC-Co cemented carbide for different binder fractions was calculated and compared with existing data [3,35]. Table 14 shows the calculated values together with experimental ones. In figures 17-19 the results for the modeling of $F(H \cdot K_{Ic})$, K_{Ic} and H are presented and the maximum and minimum values are presented in table 15. In figures 20-21 the deviation of calculated values compared to experimental ones are shown.

Table 14: Comparison of H and K_{Ic} of WC-Co cemented carbides for different binder volume and grain size. Values marked * are from experimental data.

| V_B | d | $H(\text{MPa})$ | $K_{Ic}(\text{MPa m}^{1/2})$ | $H(\text{MPa})^*$ | $K_{Ic}(\text{MPa m}^{1/2})^*$ |
|-------|-----|-----------------|------------------------------|-------------------|--------------------------------|
| 10 | 2.0 | 17155 | 13.1 | 15495 | 10.0 |
| 10.4 | 0.8 | 21100 | 13.2 | 16671 | 8.2 |
| 10.5 | 1.2 | 19500 | 13.2 | 16181 | 9.8 |
| 15 | 2.0 | 14475 | 14.7 | 14318 | 13.0 |
| 16.8 | 2.5 | 12300 | 15.2 | 13239 | 16.3 |
| 20 | 2.0 | 12500 | 15.9 | 12749 | 15.5 |

Table 15: Maximum and minimum values of $F(H \cdot K_{Ic})$ with the corresponding fracture toughness and hardness of a WC-Co cemented carbide.

| | $F(\text{MPa}^2 \text{m}^{1/2})$ | $K_{Ic}(\text{MPa m}^{1/2})$ | $H(\text{MPa})$ |
|---------|----------------------------------|------------------------------|-----------------|
| Maximum | 316×10^3 | 16.0 | 22513 |
| Minimum | 112×10^3 | 13.1 | 8445 |

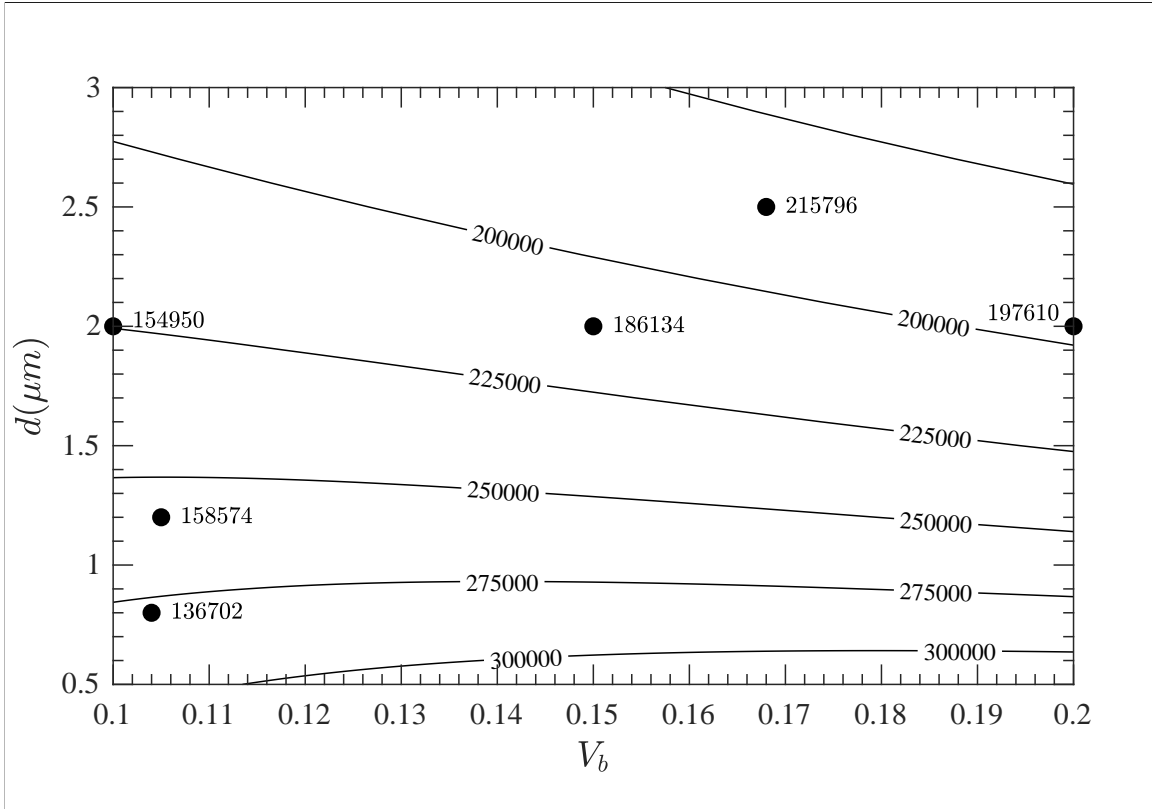


Figure 17: Calculated F values for a WC-Co cemented carbide with solid solution hardening. Contour lines indicate the value of $H \cdot K_{Ic}$. Markers indicate experimental data.

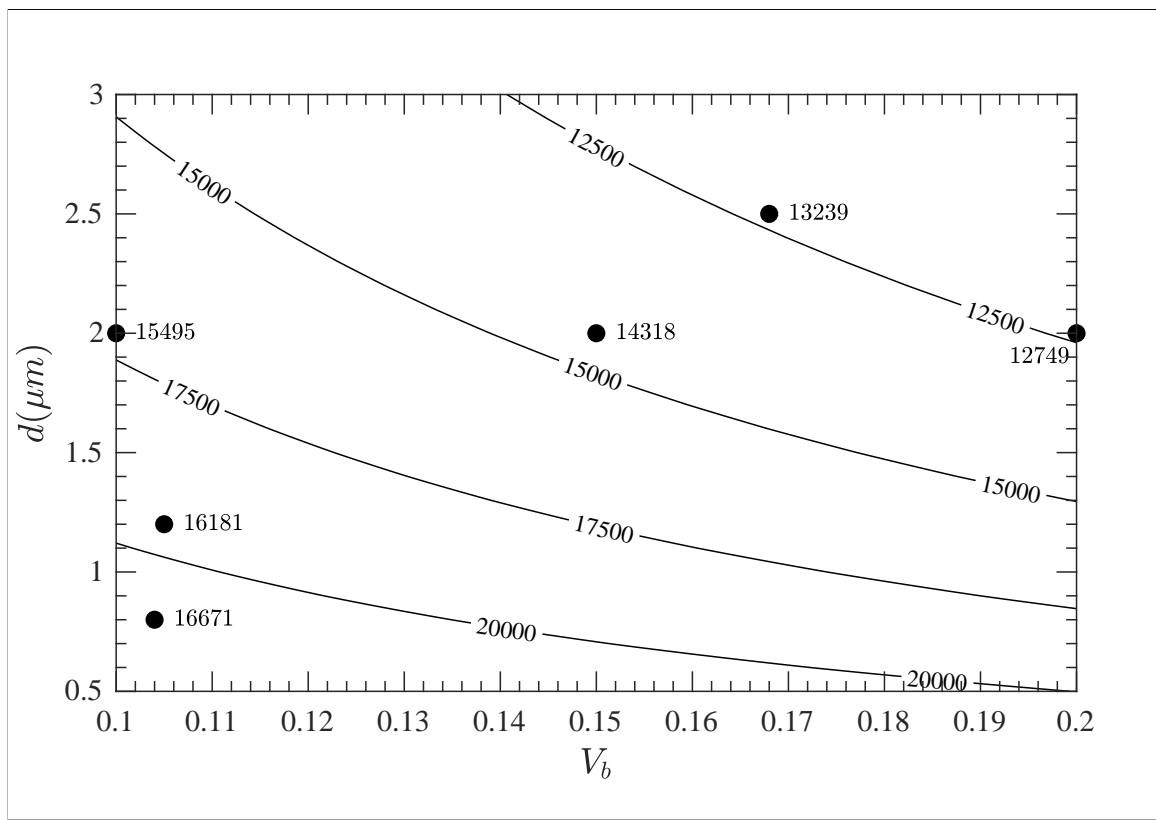


Figure 18: H values for a WC-Co cemented carbide. Markers indicate experimental data.

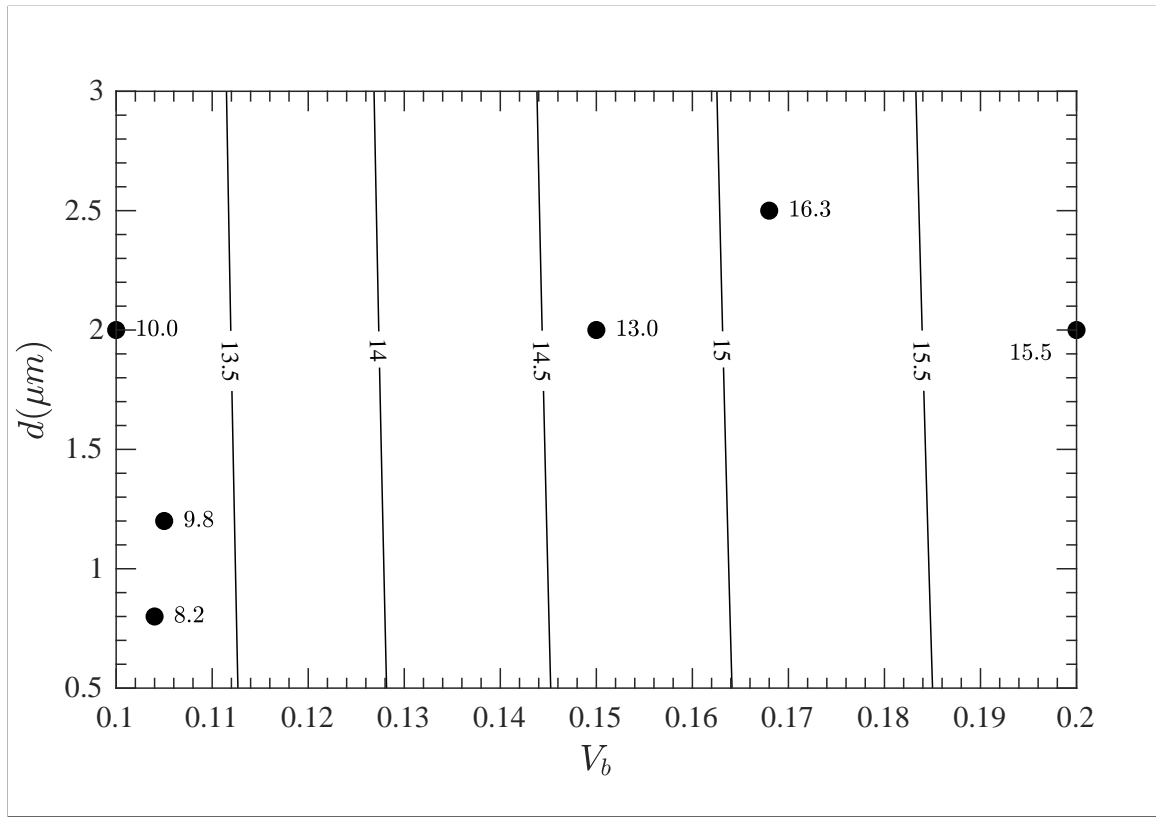


Figure 19: K_{Ic} values for a WC-Co cemented carbide. Markers indicate experimental data

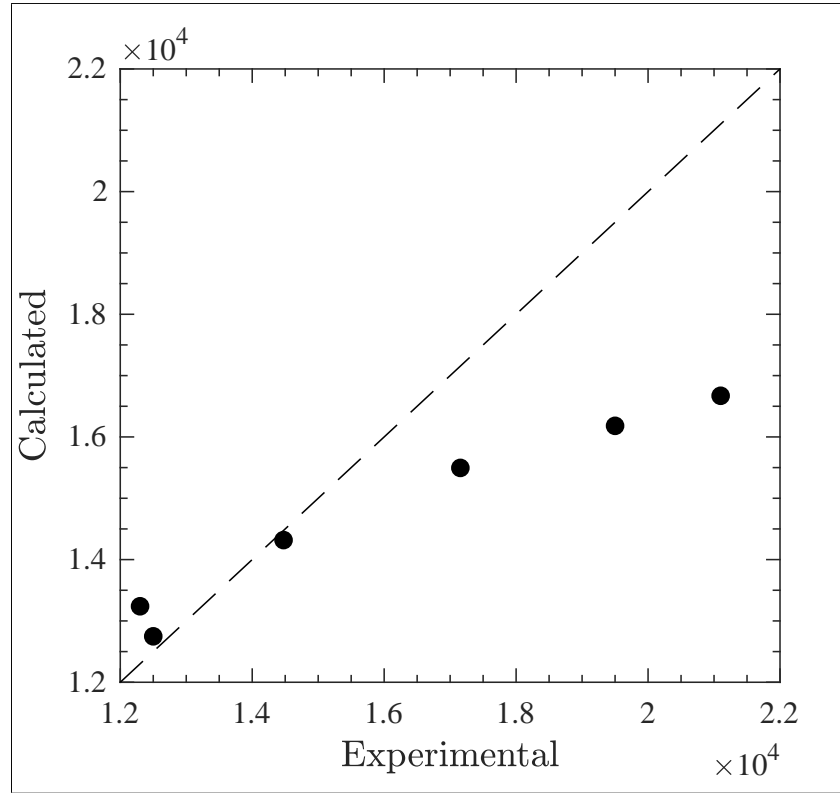


Figure 20: Comparison between calculated and experimental values of H for WC-Co cemented carbides.

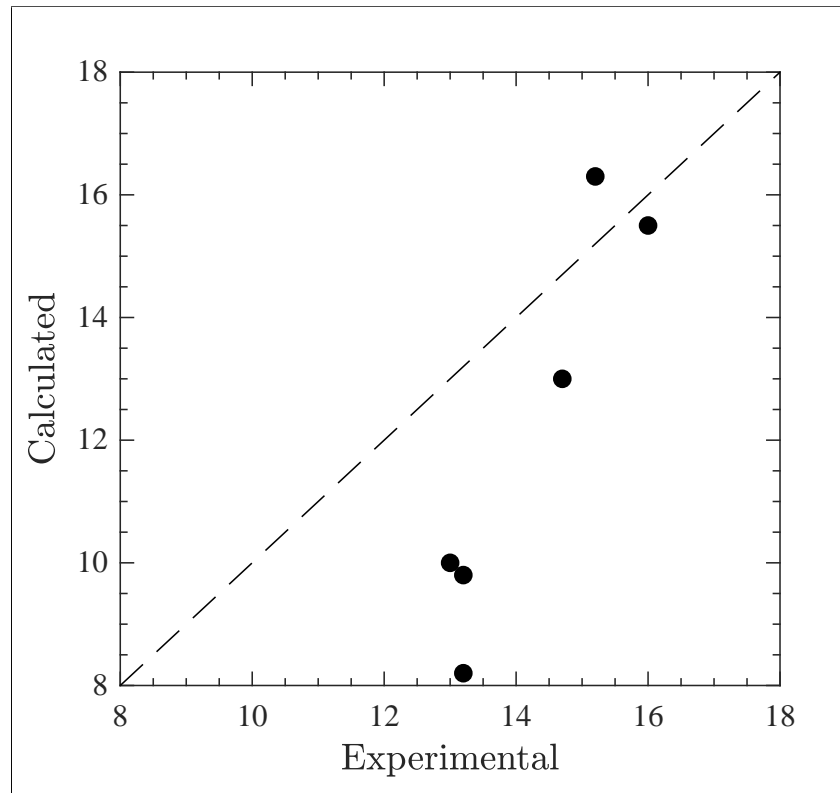


Figure 21: Comparison between calculated and experimental values of K_{Ic} for WC-Co cemented carbides.

5 Discussion

5.1 Bulk alloys

Accurately modeling the fracture toughness and hardness of bulk alloys is a complex task. The fracture toughness is a property which depends on many factors and mechanisms that are difficult to predict. In this work, the focus was mainly on void fraction and spacing. Even for the considered parameters, many simplifications had to be made. In reality, no material will contain evenly spaced voids with a fixed radius. Therefor, the void by void growth and multiple void growth mechanisms will simultaneously contribute to the fracture toughness which will likely have affected the results.

From the results in section 4.2, it is clear that the decrease in F values moving from large size and low fraction to low size and large fraction of voids is due to the rapid decrease in fracture toughness. While the decrease in hardness was only 10-15%, there was a loss of fracture toughness of 80-85%. Thus the maximum of F values coincides with the maximum of the fracture toughness. It is apparent that the fracture toughness is a much more sensitive property to the formation of voids inside the material and will likely be the controlling factor in having a good combination of material properties. It is also interesting that as the void size decreases, the contour plot seems to flatten out, indicating that for small void sizes the void fraction is less significant than for large voids.

The model verification in section 4.1 shows that the simulation results are in reasonable agreement with experimental data. However, the comparison was based on many assumptions which is a source of error. The FEM data on which the models were based was from 2-D data which can also explain the difference in fracture toughness. If a 3-D model had been used, the expression of the distance between voids would have been different, rendering slightly higher values. A comparison for a similar model with 2-D and 3-D modeling showed that 3-D results render approximately 10% higher values [17] of the required stress for the separation of voids, which would translate into higher values of the fracture toughness.

For the simulation of precipitation hardening, using equation (10) is an easy and straightforward way of determining the effects of particles on the yield strength knowing only a few parameters such as the materials shear modulus and burgers vector. The model was shown to be in excellent agreement with experimental results [21]. The solid solution hardening model was shown to have a 13% deviation from experimental results [5], which is a very good result for a model that predicts the properties of hundreds of different systems. Although the two models have shown good results as standalone models, it is not known how the two mechanisms would interact with each other. It is reasonable to assume that the formed precipitates in a bulk alloy would have an effect on the site fractions of substitutional and interstitial atoms in the matrix, thus altering the solid solution contribution. Furthermore, the ability to form particles could be affected by the presence of impurity atoms.

The likely structure transformation from FCC to BCT in a Fe-Ni-Co bulk alloy after production would influence the properties of the material. Most likely the hardness would increase at the cost of an increase of the materials brittleness. It would be possible to predict the properties in even more detail if the martensite transformation could be accurately modeled. The models in this work do not support predictions of such structure transformations.

One of the goals of this work was to further develop and integrate models for predicting the properties of bulk alloys in the Fe-Ni-Co system and verify their accuracy. While it seems that such models can be developed, it is not yet possible to completely verify them due to a lack of experimental data for the properties of bulk alloys as a function of void fraction and size.

5.2 Cemented carbides

Models that can predict the cemented carbide properties have been developed and improved for many years. The models that were used and integrated have been verified experimentally to provide reasonably accurate results. The use of the models does however require knowledge of the in situ fracture toughness of the binder, of which there exists little experimental data. Approximations of the G'_B in equation (11) based on an estimation of void fraction and size have likely affected the results. Furthermore, the available FEM data was for a material with properties $E/\sigma_y = 500$ and $n = 0.2$, which are slightly higher than those of cobalt.

The results of the simulation for cemented carbides combined with solid solution hardening provided results that showed good agreement with experimental data considering that many sim-

plifications and assumptions were made. The simulated hardness had an average deviation from experimental results of 11.5% and the fracture toughness had an average deviation of 24.8%. The best agreement with experimental results for both hardness and fracture toughness was found for the materials that had a medium to high binder volume fraction and medium to high carbide grain size. For the small volume fractions and grain sizes, the deviation was significant for both properties. There are likely size and volume factors that are not being accounted for in the presented models. Thus the crucial aspects of further developing the models will be to account for the influence of small grain sizes and low binder volume fraction.

Figures 18 and 19 show that, while it is true that an increase in hardness leads to a reduction in fracture toughness and vice versa, the relation is very much depending on grain size and binder fraction. While the fracture toughness does not seem to be heavily affected by the carbide grain size, an increase of grain size quickly leads to a decrease in the hardness. This is however not in agreement with experimental data, that showed a significant dependence on grain size for both hardness and fracture toughness [3]. Thus the experimental observations of fracture toughness do not follow the same general trend as the presented models in terms of carbide grain size.

5.3 Environmental aspects

Since it has been concluded that cobalt is toxic to humans and that it is likely that there is a connection between cobalt powder inhalation and pulmonary cancer, the effects of replacing cobalt with other binders in cemented carbides for people in the cobalt mining industry could be positive. However, compared to other industries such as the superalloys and rechargeable batteries industries, the demand for cobalt in cemented carbides is relatively small. In 2015, only 8% of the world's produced cobalt was used for cemented carbide products [36]. Figure 22 shows the global consumption of cobalt by industries. Nearly half of the produced cobalt was used for the production of batteries. How large the effects for workers handling cobalt powder globally would be by replacing cobalt in cemented carbides remains a question that needs further investigation.

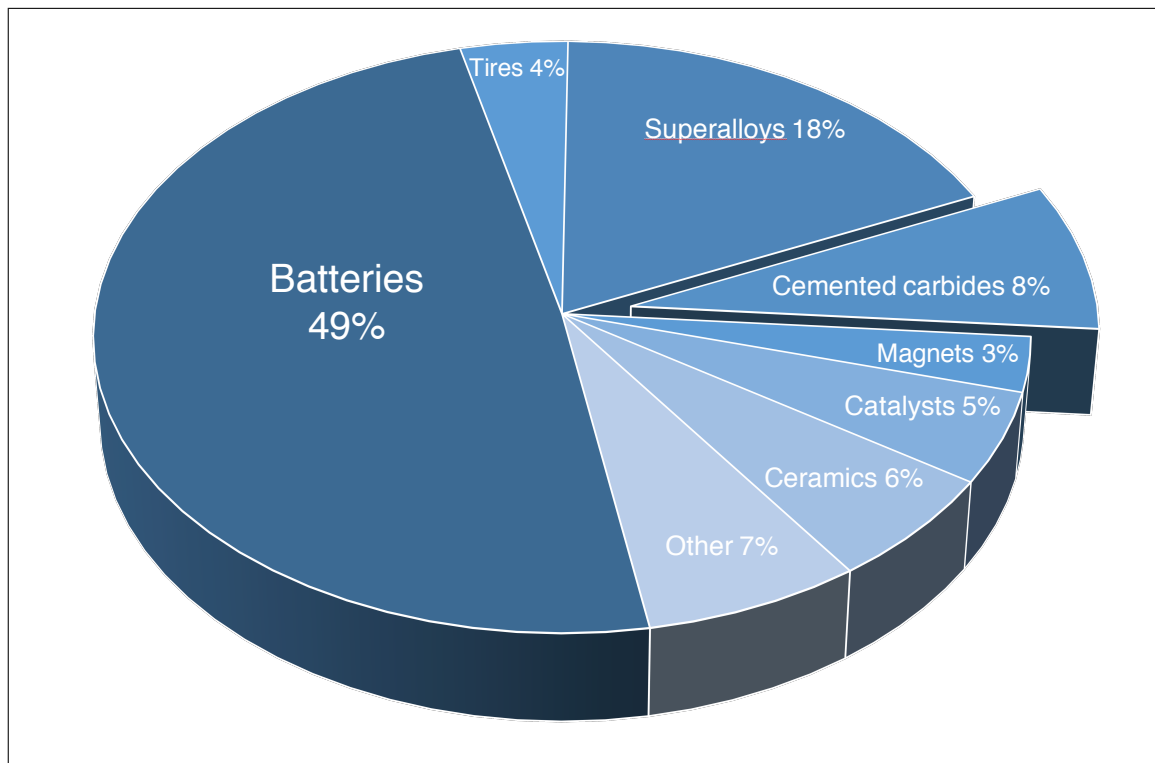


Figure 22: The figure shows how the global cobalt demand is distributed among the industries. Nearly 50% of the world's produced cobalt was used in the rechargeable batteries industry [36].

Apart from human health, the environmental aspects of choosing new materials is of great concern. For the possible replacement of cobalt as binder phase material in cemented carbides, many environmental considerations must be made. In table 16, the CO₂ footprint, water consumption and

embodied energy of production of materials 1-4 is presented. Data was gathered from CES Edupack. All of the materials have a similar CO₂ footprint, whereas the water consumption of cobalt is roughly 4-5 times higher than that of the Fe-Ni-Co alloys. Furthermore, the embodied energy, which is the sum of all energy required to produce the material, is roughly 40-70% higher for cobalt than for the rest of the materials. It is clear that cobalt is a material that requires very large resources compared to the investigated Fe-Ni-Co bulk alloys.

Table 16: Water and energy consumption together with CO₂ emissions for primary production of materials #1-4. Values marked * are estimates

| # | CO ₂ (kg kg ⁻¹) | Embodied energy (MJ kg ⁻¹) | Water consumption (l kg ⁻¹) |
|---|--|--|---|
| 1 | 7.9-8.7 | 122-134 | 553-612* |
| 2 | 6.3-6.9* | 86-95* | 126-140* |
| 3 | 5.7-6.4* | 79-88* | 107-119* |
| 4 | 5.4-6.0* | 72-80* | 107-119* |

In table 17, values for end-of-life considerations of the materials is presented. All of the materials are recyclable, with CO₂ of recycling approximately 30-50% higher for cobalt compared to the bulk alloys. The relation is roughly the same for embodied energy of recycling. It also shows that the recycling percentage of cobalt is 5% lower than for the other materials. Thus recycling considerations currently speak in favor of Fe-Ni-Co bulk alloys compared to cobalt.

Table 17: CO₂ emissions and embodied energy of recycling for materials #1-4. Values marked * are estimates.

| # | Recyclable | CO ₂ (kg kg ⁻¹) | Embodied energy (MJ kg ⁻¹) | Recycle fraction (%) |
|---|------------|--|--|----------------------|
| 1 | Yes | 1.8-2.0* | 23.1-25.5* | 23.7-26.2 |
| 2 | Yes | 1.4-1.5* | 17.7-19.5* | 28.9-31.9 |
| 3 | Yes | 1.2-1.3* | 15.5-17.1* | 28.9-31.9 |
| 4 | Yes | 1.2-1.3* | 15.5-17.1* | 28.9-31.9 |

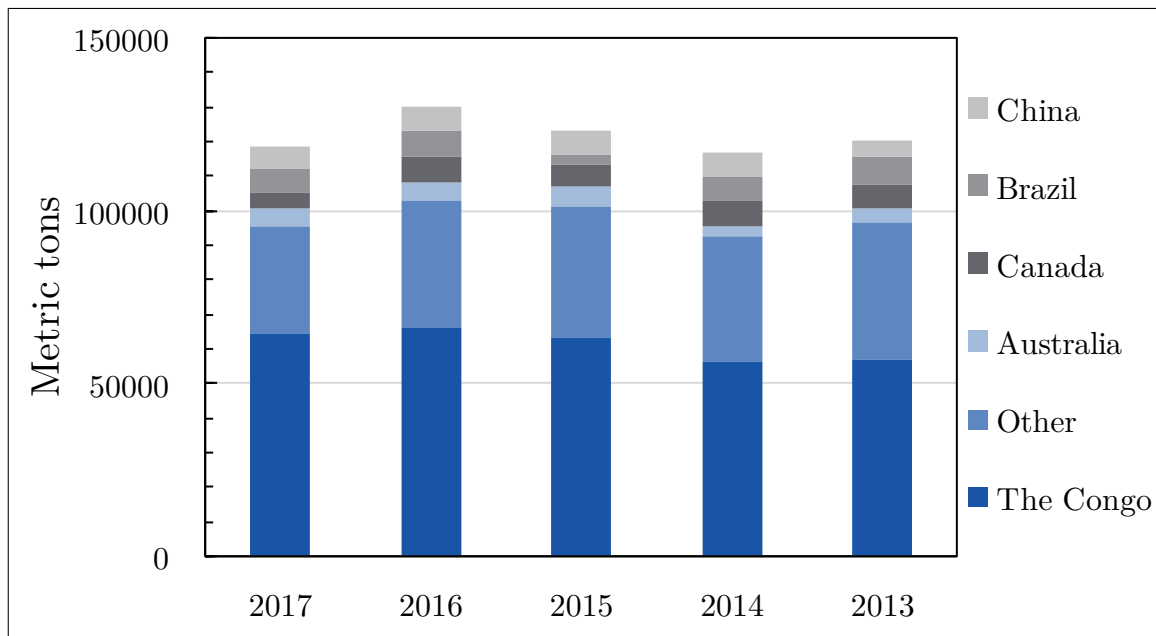


Figure 23: The figure shows the global production of cobalt by country. The Congo is responsible for approximately 60% of the worlds cobalt production [36].

6 Conclusions

The FEM based modeling approach coupled with models for solid solution hardening and precipitation hardening for the properties of bulk alloys and cemented carbides is a promising method that has potential. However, results from simulations could not be verified due to a lack of experimental data. Using a 2-D model will underestimate the results of the fracture toughness by approximately 10% compared to a 3-D model. The effects of solid solution hardening and precipitation hardening interactions is a source of error that has yet to be investigated.

For cemented carbides, the values from simulation of the fracture toughness and hardness were in good agreement with experimental data, showing an average deviation by 24.8% for fracture toughness and by 11.5% for hardness. The model shows promising results for being able to predict the properties of WC-Co cemented carbides.

The environmental aspects of replacing cobalt with Fe-Ni-Co bulk alloys would be positive, contribution to reducing the negative health concerns of workers in the cobalt mining industry while reducing the global CO₂ footprint, water consumption and energy usage.

6.1 Recommendations

For bulk alloys, future measurements of hardness and fracture toughness as a function of approximate void size and fraction are needed to verify if the models described in the report are accurate.

To investigate if the model for cemented carbide properties can be used for other binders than cobalt, experimental data is needed of fracture toughness and hardness data for WC-Fe-Ni-Co cemented carbides for different grain sizes and binder fractions is necessary to verify the validity of the model with other binders. Future studies are also required investigating the in situ fracture toughness of the binder in order to accurately predict the strain energy release rate.

Using 3-D based models would render more accurate results, especially together with models that can account for the martensitic transformation from FCC to BCT in Fe-Ni-Co alloys.

7 Acknowledgments

Firstly, I would like to thank Prof. Annika Borgenstam at the unit of structures, KTH for helping me find this project for my bachelor thesis, as well as making me interested in the subject of material structures and properties through her interesting lectures. I am happy for the opportunity to help out.

I would also like to thank Ph.D. Student David Linder at the same unit for giving me the opportunity to help him with his work. He provided excellent supervision and advice during the process of writing this report. He also gave me a lot of freedom to design the models as I deemed appropriate, which made the process much more interesting. I wish him good luck on his continued work.

I owe Prof. Anders Eliasson at the unit of processes, KTH a huge thank you as well. Although he was not directly involved in this work, he has been a constant source of knowledge and support during my time at KTH and through his passion for materials science and engineering, he has given me a lot of valuable knowledge.

Lastly, I would like to thank all the helpful people on the Mathworks community for giving great response to questions and issues regarding MATLAB®. Thanks to your tireless work, working with MATLAB® becomes much easier. Keep it up!

Also, special regards to the company Sandvik AB for being a strong driving force behind the development and investigation of new materials.

8 References

- [1] M. D. Boeck, M. Kirsch-Volders, and D. Lison, “Cobalt and antimony: genotoxicity and carcinogenicity,” *Fundamental and molecular mechanisms of mutagenesis*, vol. 533, pp. 135–152, 2003.
- [2] “Industry giants fail to tackle child labour allegations in cobalt battery supply chains,” accessed 2018/03/12. [Online]. Available: <https://www.amnesty.org/en/latest/news/2017/11/industry-giants-fail-to-tackle-child-labour-allegations-in-cobalt-battery-supply-chains/>
- [3] C. Liu, “Alternative binder phases for WC cemented carbides,” Master’s thesis, Kungliga Tekniska Högskolan, 2014.
- [4] L. R. Toller, “Alternative binder hardmetals for steel turning,” Licenciate thesis, Uppsala University, 2017.
- [5] M. Walbrühl, D. Linder, J. Ågren, and A. Borgenstam, “Modelling of solid solution strengthening in multicomponent alloys,” *Materials Science and Engineering A*, vol. A700, pp. 301–311, 2017.
- [6] N. Chopra, “Integrated Computational Materials Engineering: A Multi-Scale Approach,” *The Minerals, Metals and Materials Society*, vol. 67, pp. 1–2, 2014.
- [7] M. Wahlbrühl, “ICME guided development of cemented carbides with alternative binder systems,” Ph.D. dissertation, Kungliga Tekniska Högskolan, 2017.
- [8] K. Tsuda, “History of development of cemented carbides and cermet,” Sumitomo Electric, Tech. Rep., 2016.
- [9] S. Sheikh, R. M’Saoubi, P. Flasar, M. Schwind, T. Persson, J. Yang, and L. Llanes, “Fracture toughness of cemented carbides: Testing method and microstructural effects,” *Int. Journal of Refractory Metals and Hard Materials*, vol. 8, pp. 2–3, 2014.
- [10] A. Petersson, “Cemented Carbide Sintering: Constitutive Relations and Microstructural Evolution,” Ph.D. dissertation, Kungliga Tekniska Högskolan, 2004.
- [11] “Human rights abuses in the democratic republic of the congo power the global trade in cobalt,” accessed 2018/03/16. [Online]. Available: <https://www.amnesty.org/download/Documents/AFR6231832016ENGLISH.PDF>
- [12] “Study report on the conditions of use of five cobalt salts,” accessed 2018/03/15. [Online]. Available: https://echa.europa.eu/documents/10162/13641/cobalts_salts_study_report_en.pdf/42f0947f-e7fe-7b14-fc97-cfda0c068e9d/
- [13] H. Exner and L. Sigl, “Experimental Study of the Mechanics of Fracture in WC-Co Alloys,” *Int. Journal of Refractory Metals and Hard Materials*, vol. 15, pp. 139–149, 1997.
- [14] W. D. Callister and D. G. Rethwisch, *Materials Science and Engineering*. 111 River Street, Hoboken, NJ: Wiley, 2011, vol. 8, ISBN 978-0-470-50586-1.
- [15] X. Gao, T. Wang, and J. Kim, “Fracture and fatigue behavior of cemented carbides: 3-D FIB tomography of crack-microstructure interactions,” *International Journal of Powder Metallurgy*, vol. 50, no. 4, 2014.
- [16] X. Gao and T. Wang, “On ductile fracture initiation toughness: Effects of void volume fraction, void shape and void distribution,” *International Journal of Solids and Structures*, vol. 42, 2005.
- [17] V. Tvergaard and J. W. Hutchinson, “Two mechanisms of ductile fracture: void by void growth versus multiple void interaction,” *International Journal of Solids and Structures*, vol. 39, 2002.
- [18] R. Ritchie, “Mechanisms of fatigue crack propagation in metals, ceramics and composites: role of crack tip shielding,” *Materials Science and Engineering A*, vol. A103, pp. 15–28, 1988.

- [19] B. Uhrenius, H. Pastor, and E. Pauty, “On the Composition of Fe-Ni-Co-WC-Based Cemented Carbides,” *Metallurgical Transactions A*, vol. 18A, 1987.
- [20] H. Somekawa, Y. Osawa, and T. Mukai, “Effect of solid-solution strengthening on fracture toughness in extruded Mg-Zn alloys,” *Scripta Materialia*, vol. 55, p. 596, 2006.
- [21] T. Gladman, “Precipitation hardening in metals,” *Materials Science and Technology*, vol. 15, no. 1, pp. 30–36, 1999.
- [22] “MathWorks: MATLAB,” accessed 2018/06/19. [Online]. Available: <https://se.mathworks.com/products/matlab.html?requestedDomain=//se.mathworks.com>
- [23] “Thermo-Calc,” accessed 2018/06/19. [Online]. Available: <http://www.thermocalc.com/products-services/software/thermo-calc/>
- [24] “CES Edupack,” accessed 2018/06/19. [Online]. Available: <http://www.grantadesign.com/education/edupack/>
- [25] L. Sigl and S. Schmauder, “Finite element study of crack growth in WC-Co,” *Int. Journal of Fracture*, vol. 36, pp. 305–317, 1988.
- [26] D. Linder, J. Ågren, and A. Borgenstam, “Bridging the gap between bulk properties and confined behavior using Finite Element analysis,” KTH Royal Institute of Technology, Tech. Rep., 2002.
- [27] V. Tvergaard, A. Needleman, and A. Gurson, “Analysis of the cup-cone fracture in a round tensile bar,” *Acta metall*, vol. 32, no. 1, pp. 157–169, 1984.
- [28] D. Linder, “Fem indentation data,” to be published.
- [29] H. Engqvist, S. Jacobson, and N. Axén, “A model for the hardness of cemented carbides,” *Wear*, vol. 252, pp. 384–393, 2002.
- [30] D. Linder, “Fem fracture data,” to be published.
- [31] D. Roylance, “Introduction to fracture mechanics,” Massachusetts Institute of Technology, Cambridge, Tech. Rep., 2001.
- [32] D. Linder, “Fem thin film fracture data,” to be published.
- [33] L. Bauvineau, H. Burlet, C. Eripret, and A. Pineau, “Modelling ductile stable crack growth in a C-Mn steel with local approaches,” *Journal de Physique IV Colloque*, vol. C6, no. 6, pp. 33–42, 1996.
- [34] C. E. 2017, mar 2018, materials data.
- [35] K. Jia, T. Fischer, and B. Gallois, “Microstructure, hardness and toughness of nanostructured and conventional WC-Co composites,” *Nanostructured materials*, vol. 10, pp. 875–891, 1998.
- [36] “The importance of cobalt,” accessed 2018/05/08. [Online]. Available: <https://licoenergymetals.com/cobalt/#prettyPhoto>

9 Appendix: Coefficients from FEM simulations

Coefficients a, b, c from FEM indentation data fitting.

| Coeff. | $n =$ | 0.0 | 0.1 | 0.2 | 0.3 |
|--------|-------|---------|--------|-------|-------|
| a | | -693.93 | -24.18 | 3.84 | 1.68 |
| b | | -2.09 | -0.02 | 0.14 | 0.28 |
| c | | 2.73 | 24.99 | -3.52 | -1.48 |

Coefficients a from FEM fracture data fitting.

| E/σ_y | $n =$ | 0.0 | 0.1 | 0.2 | 0.3 |
|--------------|-------|-------|---------|---------|---------|
| 100 | | -8.28 | -10.28 | -16.51 | -22.14 |
| 500 | | 0.65 | 46.84 | -63.29 | -82.84 |
| 1000 | | 0.70 | -79.09 | -118.21 | -272.04 |
| 3000 | | 8.04 | -172.91 | -257.92 | -341.35 |

Coefficients b from FEM fracture data fitting.

| E/σ_y | $n =$ | 0.0 | 0.1 | 0.2 | 0.3 |
|--------------|-------|-------|------|------|------|
| 100 | | 0.06 | 0.19 | 0.27 | 0.28 |
| 500 | | -0.35 | 0.16 | 0.26 | 0.24 |
| 1000 | | -0.40 | 0.19 | 0.25 | 0.48 |
| 3000 | | -0.23 | 0.23 | 0.29 | 0.21 |

Coefficients c from FEM fracture data fitting.

| E/σ_y | $n =$ | 0.0 | 0.1 | 0.2 | 0.3 |
|--------------|-------|-------|--------|--------|--------|
| 100 | | 11.16 | 11.11 | 14.45 | 19.63 |
| 500 | | 8.21 | 41.03 | 48.91 | 70.61 |
| 1000 | | 12.70 | 64.08 | 85.23 | 109.36 |
| 3000 | | 12.02 | 127.90 | 180.78 | 306.40 |

Coefficients a, b, c from FEM fracture thin film data fitting. All values are for $E/\sigma_y = 500$ and $n = 0.2$.

| h | a | b | c |
|-----------|--------|--------|-------|
| $\gg x_0$ | -63.39 | 0.2557 | 48.92 |
| $25x_0$ | -52.75 | 0.2739 | 42.62 |
| $10x_0$ | -44.87 | 0.2149 | 41.28 |
| x_0 | -18.11 | 0.6372 | 19.55 |